École Polytechnique Fédérale de Lausanne

Laboratory of Quantum magnetism

Master Thesis

Neutron Scattering of Spin Waves in Square Lattice Quantum Antiferromagnets at high and low energies

Diane Lançon

Supervisor:
Prof. Henrik M. Rønnow
Assistant:
Bastien Dalla Piazza

August 10, 2012

Acknowledgements

I would like to thank Henrik Rønnow for his supervision of this master thesis work and for introducing me to the field of quantum magnetism.

My thanks also to Kruno Prsa from the LQM and Monica Jimenez from the ILL for their precious help in guiding me through my first TAS experiment. I thank also Ross Stewards and Russel Ewings from ISIS for the time they took to introduce me to neutron time of flight.

I would like to acknowledge all of the LQM lab members, and particularly Bastien Dalla Piazza, whose excellent explanations helped me understand theoretical concepts. My thanks also to Neda Nikseresht, for her support and advice.

Contents

1 Introduction

In the field of quantum magnetism, neutron scattering techniques allows probing of the magnetic properties of many materials, as the neutrons carry spin. Interesting materials are for example the parent compound of a high temperature superconductor La_2CuO_4 or the band insulator $Cu(DCOO)_2 \cdot 4D_2O$ (known as CFTD). Although the electrical properties of these two compounds are different, both show antiferromagnetic Heisenberg coupling of spin 1/2 in a 2D square lattice geometry, with very weak interplane coupling in the third direction, which implies that the magnetic properties of both La_2CuO_4 and CFTD present many similarities. In such systems, the excitations of the spins are known as spin waves, and neutron scattering has played a crucial part in better understanding this theory, as it gives the possibility to directly probe the correlation functions describing the system. However, the compounds have also been found to have non classical and highly fluctuating behaviour, due to the quantum nature of spin 1/2 spins and the low dimensionality antiferromagnetic system. The aspects of the two compounds studied in this work are as follows :

La_2CuO_4 is the parent compound of a High-T_c superconducting cuprate which is obtained by chemical hole doping that rapidly destroys the antiferromagnetic order present in La_2CuO_4 . One of the great challenge of solid state physics is to understand how doping the antiferromagnetic planes of cuprates with holes can lead to superconductivity with such high transition temperatures.

In the undoped compound, the renormalised classical spin wave theory that reproduces the overall profile of the dispersion spectrum fails to explain the deviation from that theory at the zone boundary. This deviation was observed using neutron scattering, thanks to significant improvements of the flux and design of neutron time of flight spectrometer. This particular anomaly was also observed on CFTD, which gives hints that non classical behaviour characterises the 2D square lattice quantum antiferromagnet.

In order to study the high energy anomalous lineshape at the $Q = (\pi, 0)$ point of the zone boundary, this work will be concerned with the preparation and realisation of a triple axis spectrometer experiment. Obtaining such a method to investigate the anomaly would allow further studies on lightly doped compounds. The advantage of the triple axis is that it allows mapping of particular points of Q-space with high resolution, which has a time and precision advantage over mapping the entire excitation spectrum. The optimal choice of experimental configuration for the hot neutron spectrometer IN1 will be investigated in details in this work. Indeed, the

follow up goal would be to investigate how magnetic excitations evolve when antiferromagnetic order is suppressed by a gradual doping of the cuprate. To this end, one must first start with the undoped compound to evaluate whether it is possible to design a TAS experiment that detects the anomaly. The difficulty of accessing large energy transfers will be addressed in this work, as the maximum of the dispersion is around 300 meV. One of the step to limit the impact of such high energy transfer is the use of neutron resonance filters, which will be discussed in details. Indeed, the need to possess reliable data on filter materials to limit spurious signals led us to conduct an additional experiment to facilitate the design of the La_2CuO_4 neutron scattering experiment.

In the case of the $Cu(DCOO)_2 \cdot 4D_2O$ compound, the aspect studied in this work is the anisotropy of the nearest neighbour intra plane exchange constant J. If the model Hamiltonian of the system is taken to be an isotropic Heisenberg nearest neighbour Hamiltonian, it would lead to magnetic excitation which present Goldstone modes. However neutron scattering experiments have shown that there are energy gaps opening, which means one should consider the nearest neighbour exchange constant J as anisotropic. In this study are presented the analysis of such an experiment that allows extraction of the anisotropy coefficients through measurements of the magnetic excitations. In the case of CFTD, the energy of the magnetic excitation is much lower than in the La_2CuO_4 case, as the dispersion has a maximum of 14 meV energy transfer, so that the experiment was performed on a cold neutron triple axis spectrometer.

Before moving on to the particular studies presented above, the first part of this project will introduce some theoretical background on high Tc cuprates related to the studied La_2CuO_4 as well as on the model of 2D square lattice Heisenberg antiferromagnets and the deviation from the spin wave dispersion. A short introduction to neutron scattering concepts and techniques will also be given, in particular in the case of magnetic studies.

2 High Tc cuprates and square lattice Quantum Antiferromagnets

2.1 High-Tc Superconductivity in Cuprates

High Tc superconductors are compounds which are superconducting at particularly high temperature (For example, $HgBa_2Ca_2Cu_3O_x$ is a superconductor with a transition temperature T_c of 135 K at ambient pressure [1]), compared to conventional superconductors, for which, according to the BCS theory, T_c is limited to 30K.

High Tc superconductivity can be found in cooper oxide compounds, known as cuprates, which possess a CuO_2 plane as their structural unit. Such compounds are antiferromagnetic Mott insulators at zero doping, but have a superconducting phase upon hole doping or electron doping.

As opposed to a conventional band insulator (filled energy band), it is electron-electron repulsion that prevents charge conductivity in Mott insulators due to the energy cost U of creating a double electron site. This is described by the one band Hubbard model :

$$H = \frac{1}{2}\sum_{i,j,\sigma} t_{ij} c^{\dagger}_{i\sigma} c_{j\sigma} + U \sum_{i} n_{i\uparrow} n_{i\downarrow} \tag{1}$$

with t the electron hopping integral between the i and j sites. In the Mott insulator case, U is much larger than t. Charge is thus localized, but the spin degrees of freedom are not similarly restricted, leading to virtual hopping via super-exchange interaction, which is possible when spins are anti-parallel. Upon hole doping, conductivity is restored as electrons can jump to another site without increasing Coulomb energy.

$La_{2-x}Sr_xCuO_4$ is one of the first high T_c superconductor to be discovered, with a T_c of 38K upon hole doping of the parent compound La_2CuO_4 .

The electronic structure of a free Cu ion is $[Ar]3d^{10}4s^1$. In the parent compound La_2CuO_4 , the cuprate's $Cu0$ planes are present, and the valence of Cu is 2+, meaning that the electronic state is in the d^9 configuration. The crystal field effect splits the five d-orbitals into the t_g and e_g energy levels ([2]).

Figure 1 shows the structure of the La_2CuO_4 compound. Its octahedral environment is distorted due to the two apical oxygen atoms and this splits the e_g orbitals so that the highest partially occupied d orbital is $x^2 - y^2$. The lobes of this orbital are directed towards the p orbital of the oxygen atoms.

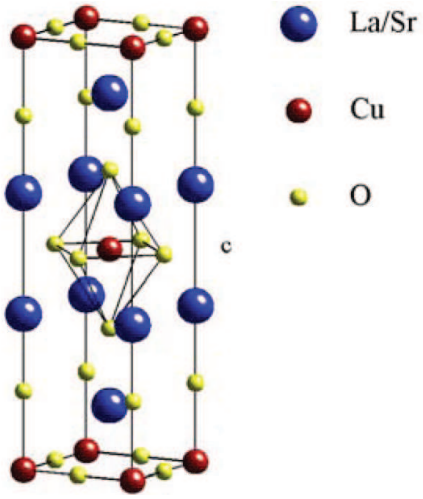

Figure 1: Unit cell of $La_{2-x}Sr_xCuO_4$, reproduced from [3]. The $Cu0_6$ octahedron is visible in the center

Upon doping with divalent Sr, which locally replaces trivalent La, holes are introduced in the CuO layer. A doping of x corresponds to the compound $La_{2-x}Sr_xCuO_4$, and thus x holes per Cu atom. The doped hole resonates on the four oxygen sites and the spin of the hole forms a spin singlet (Zhang-Rice singlet) by combination with the Cu spin, which can hop from site to site. When doping reaches a certain level, and with a temperature below Tc, antiferromagnetism is degraded and superconductivity appears. In the case of $La_{2-x}Sr_xCuO_4$it is around $x = 0.055$, with optimum doping at $x = 0.16$. Figure 2 shows a schematic phase diagram for $La_{2-x}Sr_xCuO_4$.

This phase diagram is similar in all cuprates as it generally presents four regions corresponding to an antiferromagnetic phase, a pseudo-gap phase, a superconducting phase and a Fermi liquid phase (ref. [4]). In some cuprates compounds, these regions are also present upon electron doping, and in that case the antiferromagnetic phase usually extends to higher doping values.

At zero doping, the parent compound La_2CuO_4 has a Néel temperature of 320 K. Upon hole doping, the antiferromagnetic phase disappears at very low doping levels ($x \simeq 0.02$ in $La_{2-x}Sr_xCuO_4$) and the superconducting phase appears around $x = 0.055$. The superconducting transition temperature then increases as the doping level increases up to the optimal doping point at $x = 0.16$ for $La_{2-x}Sr_xCuO_4$, before decreasing again to zero. Doping levels below the optimal doping corresponds to an underdoped compound, while higher doping levels corresponds to an overdoped

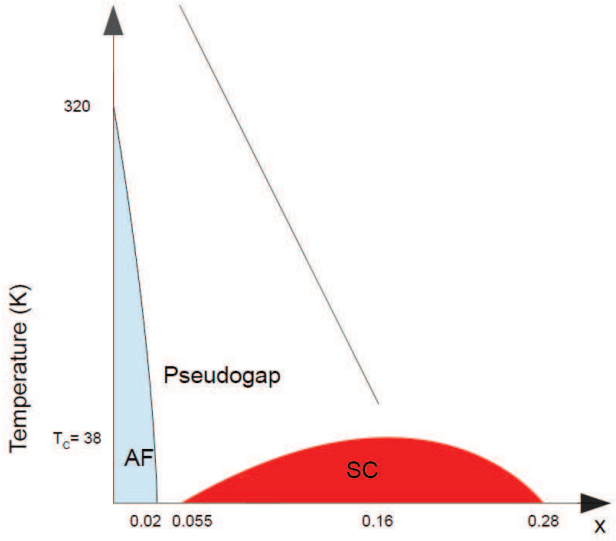

Figure 2: Cuprate phase diagram in the case of $La_{2-x}Sr_xCuO_4$, with hole doping x. AF is the antiferromagnetic phase (with Mott Hubbard model), and SC is the superconducting phase, with optimal doping at $x = 0.16$

compound.

The region outside of the superconducting state on the underdoped side corresponds to a pseudogap phase, with a number of cross over phenomena (including gradual gap opening), which have been probed using experimental techniques. Finally, when hole concentration exceeds $x = 0.28$, a normal Fermi liquid state is recovered.

2.2 Spin 1/2 square lattice Heisenberg Antiferromagnet

When undoped, La_2CuO_4 is a Mott insulator that can be considered as a two-dimensional anti-ferromagnetic system due to the spatially anisotropic coupling. Indeed, there is a strong exchange coupling within the CuO_2 plane while spins of neighbouring planes undergo weak coupling. Super exchange interaction favours anti-parallel spin alignment leading to commensurate antiferromagnetic order below the Néel temperature.

La_2CuO_4 is a realisation of a spin 1/2 square lattice Heisenberg Antiferromagnet

(SLHAF), which in the simplest model is described by the Heisenberg Hamiltonian :

$$H = J \sum_{<i,j>} \mathbf{S}_i \cdot \mathbf{S}_j \tag{2}$$

with J the Antiferromagnetic exchange constant and where $< i, j >$ corresponds to a pair of nearest neighbours. Here we restricted the interaction to nearest neighbours only, but as described below, higher order coupling must be added to reproduce the magnetic excitations in the case of La_2CuO_4 .

The dispersion relation can be derived using the spin wave theory (SWT) calculations with the assumption of non interacting magnons (Linear SWT), by rewriting the operator as Bosonic operators and diagonalising the obtained form (derivation in [3]). The obtained energy dispersion is :

$$w^A_{\mathbf{q}} = zJS\sqrt{1 - \gamma^2_{\mathbf{q}}} \tag{3}$$

Where z is the number of nearest neighbours and $\gamma_{\mathbf{q}} = \frac{1}{z}\sum_{\boldsymbol{\delta}} \exp i\mathbf{q} \cdot \boldsymbol{\delta}$, in which δ sums over to the nearest neighbour vectors.

In the 2 dimensional case where $z = 4$ and with a spin 1/2 system, the constant becomes $2J$. The dispersion is gapless, and has a maximum of $2J$ along the antiferromagnetic zone boundary (dashed line in the Brillouin zone of figure 4).

The obtained Bosonic excitations are known as spin waves, corresponding to a spin precession around the direction of the moments, and are also considered as quasiparticles (magnons). However, the Linear SWT assumption only holds at large spin values, and with spin 1/2 compounds magnon-magnon interactions must be included. Calculating quantum correction to linear spin wave theory to include interaction between spin waves yields a renormalisation constant of the dispersion over all of the $2D$ Q-space, so that fitting of the spin wave model to the dispersion measured by neutron scattering will be adjusted using a renormalised effective exchange $J_{eff} = Z_c J$.

In the case of La_2CuO_4 however, higher order interactions must also be included in order to reproduce the measured dispersion, where the spin wave energies at $(\pi, 0)$ ans $(\pi/2, \pi/2)$ are not equal. Indeed this feature does not appear when only nearest neighbour interaction is considered in the model. For the SLHAF La_2CuO_4 compound, the Heisenberg model that describes the spin wave dispersion (shown in fig 4) includes J, J', J'' the first, second and third order nearest neighbour and J_c the ring exchange interaction that couples 4 spins, and with a renormalisation constant $Z_c = 1.18$ (equation reproduced from [6]) :

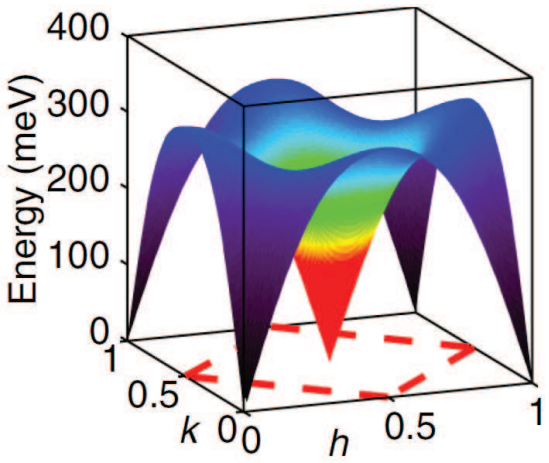

Figure 3: La_2CuO_4 dispersion from spin wave theory, reproduced from [5]

$$H = J \sum_{<i,j>} \mathbf{S}_i \cdot \mathbf{S}_j + J' \sum_{<i,i'>} \mathbf{S}_i \cdot \mathbf{S}_{i'} + J'' \sum_{<i,i''>} \mathbf{S}_i \cdot \mathbf{S}_{i''} + J_c \sum_{<i,j,k,l>} [(\mathbf{S}_i \cdot \mathbf{S}_j)(\mathbf{S}_k \cdot \mathbf{S}_l) + (\mathbf{S}_i \cdot \mathbf{S}_l)(\mathbf{S}_k \cdot \mathbf{S}_j) - (\mathbf{S}_i \cdot \mathbf{S}_k)(\mathbf{S}_j \cdot \mathbf{S}_l)] \tag{4}$$

La_2CuO_4 Crystallographic characteristics and unit choice

Below 420 K, La_2CuO_4 undergoes a phase transition from a tetragonal crystal lattice with space group $I4/mmm$ to a base centred orthorhombic lattice with space group $Cmca$. The magnetic moments are along the orthorhombic [010] axis. However, the difference between the orthorhombic axis a and b (5.375 Å and 5.409 Å) is very small and we can consider the structure to be a square lattice structure, which allows us to work in the tetragonal unit cell, with $a = b = 3.83$ Å and $c = 13.31$ Å.

Throughout this work, the wavector $\mathbf{Q}$ is specified in the reciprocal lattice of the tetragonal lattice, so that an antiferromagnetic Bragg peak with $\mathbf{Q} = (1/2\ \mathbf{a}^* + 1/2\ \mathbf{b}^* + 0\ \mathbf{c}^*)$ will be denoted $Q = (\pi, \pi)$ in the 2D square lattice reciprocal space.

2.2.1 Other realisation of square lattice Heisenberg Antiferromagnet

Another compound that realises the spin 1/2 SLHAF is $Sr_2CuO_2Cl_2$. The full magnetic spectrum of this compound was measured using Resonant Inelastic X-Ray

scattering [7]. The measured zone boundary dispersion can be well reproduced by a Hubbard model extended to further neighbour hopping, which means that J, J' and J'' exchange interaction constants should be taken into account.

The metal-organic compound $Cu(DCOO)_2 \cdot 4D_2O$, referred to as CFTD, is also a realisation of a spin 1/2 square lattice Heisenberg Antiferromagnet, with a accurate reproduction of the spin wave dispersion by the nearest neighbour Heisenberg Hamiltonian of LWT, renormalised by Z_c. CFTD's crystal structure at low temperature is monoclinic, with $P21/n$ space group and lattice parameters $a = b = 8.113$ Å, $c = 12.45$ Å, and with $\beta = 100.79°$. The Cu^{2+} ions are arranged in nearly square lattice planes parallel to the a and b axes which are separated by layers of heavy water. The inter plane exchange coupling is 10^4 fold lower than the nearest neighbour exchange interaction J, allowing it to be considered a 2D compound in terms of magnetic excitations.

2.3 The anomaly in CFTD and La_2CuO_4 dispersion

Although there is a good general agreement between spin wave theory and experimentally obtained dispersion for the square lattice Heisenberg anti-ferromagnet compounds, further experimental studies of the spin dynamics with improved resolution have shown the existence of a zone boundary anomaly at the $(\pi, 0)$ point of the Brillouin zone.

This anomaly is characterised by a reduction of the magnon energy, a drop in the one magnon amplitude, and an anomalous energy line-shape with a transfer of spectral weight to higher energy at $Q = (\pi, 0)$. These characteristics have been seen on CFTD (ref [8]), where the magnon energy is reduced by 7% and where there is a 40% drop in intensity.

It was also observed with the La_2CuO_4 compounds, using a time of flight spectrometer to map a large area of the Brillouin zone (ref. [5]). Figure 4 shows the anomalous excitation spectrum measured in this experiment, and the agreement with spin wave theory for the other points of the dispersion. They report strongly reduced peak intensity, and a high energy tail to the magnetic excitation which cannot explained by two magnons continuum.

To explain this discrepancy between the bosonic excitations of spin wave theory and the observed experimental continuum at $(\pi, 0)$, a link can be made with the continuum in energy excitation spectrum observed in the 1D antiferromagnetic spin

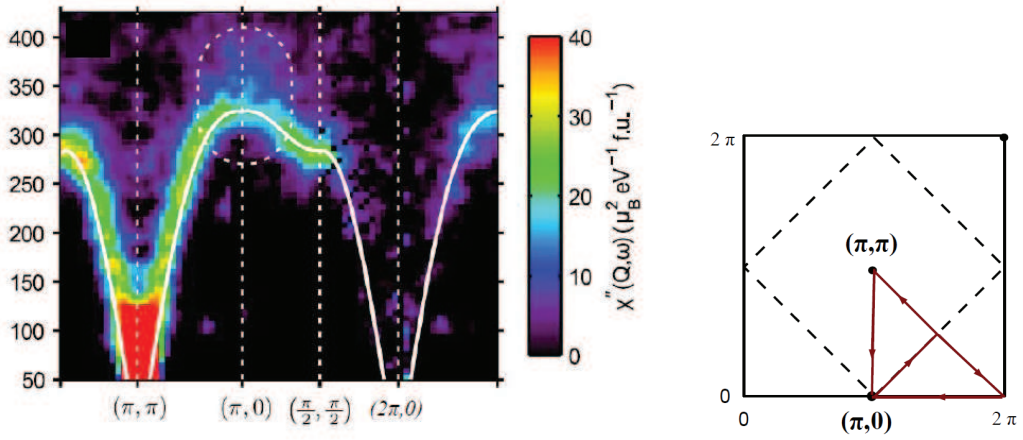

Figure 4: Left : Color map of the La_2CuO_4 dispersion spectrum, reproduced from [5], where the solid line is a spin wave theory fit based on the Heisenberg Hamiltonian (eq. 4). Right: path of the dispersion on the brillouin zone.

1/2 Heisenberg chain, such as $CuSO_4 5D_2O$ for example. Starting with the one band Hubbard model that leads to an Heisenberg model in the small t/U limit, there exists an exact solution (from Bethe ansatz), in which the ground state does not have long range order and where two quantum numbers are needed to describe the magnon spectrum. They correspond to two spin 1/2 fermions, referred to as spinons (from [9]). In 1D, the continuum of the magnon excitation spectrum thus comes from a fractionalisation of the bosonic excitation into two fermionic degrees of freedom. This model reproduces well the experimental continuum seen in the 1D chain compound $CuSO_4 5D_2O$ ([10]).

In 2D SLHAF however, there is no exact solution, but an hypothesis is that the excitations are also decoupled into spinons, with the magnetic order of the ground state (Néel order and resonant valence bond fluctuations) confining the spinons by pairs, which could possibly explain the anomaly observed in neutron scattering at the $(\pi, 0)$ point.

Therefore, the idea behind the La_2CuO_4 experiment is to define a procedure to scan the high energy excitation anomaly using a hot triple axis spectrometer on the undoped La_2CuO_4, in order to find out by further similar experiments on slightly doped compounds whether this anomaly is still present, as a possible precursor of superconductivity.

3 Neutron scattering technique

Neutron scattering is a tool that allows probing of structural and magnetic properties of materials. Because of their magnetic moment, neutrons are sensitive to the local magnetic moments in solids, and as they are not charged, they interact weakly with solids, allowing the bulk of samples to be probed.

The neutron finite magnetic moments interacts with the orbital and spin angular momentum of unpaired electrons in magnetic systems via the dipole-dipole interactions and this can be used in inelastic scattering to study magnetic excitations via spin correlation functions.
The characteristics of an neutron scattering experiment is as follows ([11]) :

An incident neutron beam of wave vector k_i and energy $E_i = \hbar^2 k_i^2/2m$ is scattered from a sample with a wavenumber k_f and energy E_f. The momentum and energy transfers that took place in the experiment are defined as : $\mathbf{Q} = \mathbf{k}_i - \mathbf{k}_f$ (momentum transfer) and $\hbar w = E_i - E_f$ (energy transfer).

As figure 5 shows, 2θ is defined as the angle between the incident and outgoing neutron beam, which forms the scattering triangle.

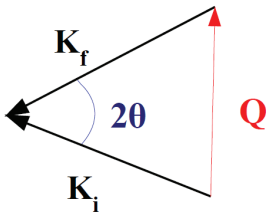

Figure 5: Scattering triangle

3.1 Scattering cross-section

The quantity measured in a neutron scattering experiment is the cross section σ, which characterises the rate of scattered neutrons per incident flux unit Ψ_0. The rate of neutrons scattered in a solid angle $\Delta\Omega$ with final energy between E_f and $E_f + \Delta E_f$ is given by :

$$I = \Psi_0 \left(\frac{d^2\sigma}{d\Omega dE_f} \right) \Delta\Omega \Delta E_f \tag{5}$$

with $\left(\frac{d^2\sigma}{d\Omega dE_f}\right)$ the partial differential cross-section. With $V(\mathbf{Q})$ the Fourier transform of the scattering potential that cause the transition from λ_i to λ_f , which can be either nuclear or magnetic, the partial differential cross section is written as :

$$\left(\frac{d^2\sigma}{d\Omega dE_f}\right)_{\lambda_i\to\lambda_f} = \frac{k_f}{k_i}\left(\frac{m_n}{2\pi\hbar^2}\right)^2 |\langle \mathbf{k}_f\lambda_f|V(\mathbf{Q})|\mathbf{k}_i\lambda_i\rangle|^2\delta(E_{\lambda i} - E_{\lambda f} + \hbar\omega) \quad (6)$$

Depending on the interaction potential, this can be used to calculate the differential cross section in either nuclear or magnetic scattering. In both cases, one can study elastic ($\hbar\omega = 0$) or inelastic scattering, with $\delta(E_{\lambda i} - E_{\lambda f} + \hbar\omega)$ the energy conservation term.

3.2 Magnetic cross section

The differential cross section associated with magnetic scattering is given by ([11]):

$$\left(\frac{d^2\sigma}{d\Omega dE_f}\right) = \frac{k_f}{k_i}(\gamma r_o)^2 \left|\frac{gf(\mathbf{Q})}{2}\right|^2 e^{-2W(\mathbf{Q}))} \sum_{\alpha\beta}(\delta_{\alpha\beta} - \hat{\mathbf{Q}}_\alpha\hat{\mathbf{Q}}_\beta)S^{\alpha\beta}(\mathbf{Q}, w) \quad (7)$$

with $S^{\alpha\beta}(\mathbf{Q}, w)$ the dynamic structure factor given by the Fourier transform of the time dependent spin-spin correlation function.

$$S^{\alpha\beta}(\mathbf{Q}, w) = \frac{1}{2\pi\hbar}\sum_{jj'} e^{-i\mathbf{Q}\cdot(\mathbf{r}_j - \mathbf{r}_{j'})}\int_{-\infty}^{\infty} e^{-iwt}dt\langle S_j^\alpha(t)S_{j'}^\beta(0)\rangle \quad (8)$$

$\hat{\mathbf{Q}}$ is the unit vector parallel to the scattering vector $\mathbf{Q}$

$\sum_{\alpha\beta}(\delta_{\alpha\beta} - \hat{\mathbf{Q}}_\alpha\hat{\mathbf{Q}}_\beta)$ thus corresponds to the geometric polarization factor. It shows that the magnetic moment of an atom contributes to the scattered intensity if this moment has a component perpendicular to $\mathbf{Q}$.

The cross section is proportional to the dynamic structure factor apart from the magnetic form factor $|f(\mathbf{Q})|^2$. This cannot be neglected in certain ions such as Cu^{2+} where strong anisotropies play a significant role when $|Q|$ increases.

$S^{\alpha\beta}(\mathbf{Q}, w)$ is connected to the imaginary part of the generalized magnetic susceptibility χ''. They are related by the fluctuation-dissipation theorem :

$$S^{\alpha\beta}(\mathbf{Q}, w) = \frac{\chi''}{1 - exp(-\hbar w/k_B T)} \quad (9)$$

This relation allows comparison of neutron scattering experimental data with theoretical models.

3.3 Neutron Source

A neutron source can either be a nuclear reactor or a spallation source. The continuous neutron source neutron used in the La_2CuO_4 experiment were produced in the HFR nuclear reactor of the ILL in Grenoble (France), where thermal neutron (10-100 meV), hot and cold neutron beams can be produced. In order to attain the required high energy transfers, a hot neutron source was necessary in our case, as it allows the production of a beam with a shift of the Maxwellian distribution of the neutrons to higher energies (up to about 800 meV).

For the time of flight filter experiment, the neutron source was the ISIS spallation source (Rutherford Appleton laboratory), in Ditcot, UK.

3.4 Triple axis spectrometer

A triple axis spectrometer allows controlled measurement of the scattering function $S(\mathbf{Q}, w)$ at a specific point in momentum ($\hbar\mathbf{Q}$) and energy ($\hbar w$) space.

In a triple axis experiment, the path of the neutrons is kept in the scattering plane (horizontal plane) and determined by three angles : monochromator, sample and analyser angles. Bragg scattering at a monochromator allows direct the selection of the wavenumber k_i of the incoming beam along with the higher order neutrons. Similarly, the analyser sends the neutron with the appropriate k_f and higher orders to the detector, according to Braggs law. At the sample, the beam is scattered with direction, spin and energy distributions determined by the spin dependant partial differential cross section. This set up thus allows the determination of the momentum transfer $\hbar\mathbf{Q}$ and energy transfer $E_i - E_f = \hbar w$ due to inelastic scattering ([12]).

Typically, either Q scans or Energy scans are performed on a triple axis. In energy scans at a given Q point, the scattering triangle is modified for each point of the scan by varying the 2θ angle, and either k_i or k_f, to obtain the requested energy transfer while keeping Q constant. On the other hand, in Q-scans, the energy transfer is kept constant. This technique is well suited to obtain information on excitation at a particular point of the Q space, or along a particular direction in ($\mathbf{Q}$,ω) space.

Either cold, thermal or hot neutrons spectrometer can be used in neutron facilities. As the monochromator and analyser crystal diffract the wanted wavelength as

well as the unwanted harmonics, spurious effect can be expected in all three cases. For hot neutrons, resonance absorption filters can be used, while for thermal neutrons, pyrolithic graphite allows the selection of two particular wavelengths while removing all other spurious signal. For cold neutrons, polycrystalline beryllium transmits only neutrons with the wavenumber below 1.57 $Å^{-1}$. Other possibilities can also be exploited to remove spurions, such as silicon or germanium crystal for example.

3.4.1 Resolution

Independently of the scattering function, the measured parameters such as k_i, k_f and 2θ are distributed around their average value, due to finite precision of the spectrometer elements such as the monochromator, the collimators or the analysers.
This leads to a distribution of the results $(\mathbf{Q}, w)$ around the average value $(\mathbf{Q}_o, w_o)$. This distribution is known as the spectrometer resolution function $R(\mathbf{Q}-\mathbf{Q}_0, w-w_o)$ (ref. [13])

As a consequence, the measured intensity can de described as a 4D convolution of the scattering function $S(\mathbf{Q}, w)$ with the spectrometer resolution function :

$$I(\mathbf{Q}_o, w_o) = \int d\mathbf{Q}dwR(\mathbf{Q}-\mathbf{Q}_0, w-w_o)S(\mathbf{Q}, w) \tag{10}$$

The resolution function can be expressed as a Gaussian distribution ([13]).

$$R(\mathbf{Q}-\mathbf{Q}_0, w-w_o) = R_0 e^{(-\frac{1}{2}\Delta v M \Delta v)} \tag{11}$$

On a triple axis spectrometer, the resolution matrix M is dependent on the parameters of the monochromator and analyzer, their mosaicity, the collimation as well as the mosaic spread of the sample itself. This leads to a 4D resolution ellipsoid (3D in Q space, and Energy) whose size and orientation depends on the resolution matrix M, and thus on the sample and instrument parameters. The principal axis of the resolution ellipsoid are usually not aligned with the Q vectors, as the matrix M is generally not diagonal. Knowledge of the resolution ellipsoid can be very useful for the data analysis of a neutron experiment.

3.5 Time of flight spectrometer

Time of flight spectrometers may be used to explore large areas of $(\mathbf{Q}, \omega)$ space as neutrons are simultaneously collected over a wide range of neutron energies. Such instruments require a pulsed neutron beam, as the neutrons velocities and energies

are determined by their time of flight to the detector. All neutrons of a given pulse are created at the same time t_0, and from the De Broglie relation, neutrons with different energies (and hence different wavelengths) travel at different velocities : $\lambda = h/mv$

For elastic scattering, such as with the ALF spectrometer experiment, the sample receives a white beam of neutrons, which get scattered into detectors.

On the other hand, for inelastic scattering, time of flight is not sufficient to determinate the energy transfer, and the TOF spectrometers thus have either a direct of indirect geometry. With direct geometry, a Fermi chopper selects a neutron energy form the white beam, and thus monochromates the beam before the sample. In indirect geometry, the energies of the scattered neutron are analysed after the sample.

4 Measurement of Neutron Absorption Resonances Filters

Neutron absorption resonance filters are materials that are characterised by sharp resonance peaks in the absorption cross-section at particular neutron energies, and low absorption cross section outside of the resonance. They are particularly useful in hot neutron experiments in order to reduce spurious signals and background by filtering out unwanted neutron energies. It could be particularly useful for the La_2CuO_4 experiment on the hot neutron triple axis IN1 at the ILL, where spurious signal should be limited as much as possible.

In this chapter, systematic comparative transmission measurements of eight neutron resonance filters are presented: Erbium, Indium, Iridium, Dysprosium, Hafnium, Gadolinium, Cadmium and Samarium. First we report already available data obtained from several database. Indeed, some materials such as Cadmium and Gadolinium are already used to block neutron beams [14]. In our experiment's case, the eight resonant filters were measured in order to obtain reliable transmission data over a wide range of neutron energies, from 1 meV to 10 eV, that are then used in the second part of this chapter to assess the calculated cross-section from the database [15].

A time of flight approach was particularly suited for these measurements, as it allowed to measure simultaneously each filter transmission for the full available neutron energy spectrum. Further analysis of the data yielded precise information on each material's first resonances energies and their characteristics in order to give insights in the design of a thermal or hot neutron experiment such as the La_2CuO_4 experiment, which requires the choice of a filter.

4.1 Available database

Two databases gave preliminary information on the filter's absorption cross-sections, and both of them yield similar values for the position of the first resonance peak : the IN1 database, obtained from the ILL, and the Evaluated Nuclear Data Library (ENDF [15]).

Calculated neutron absorption cross sections for each isotope of the filter elements could be found in the EDNF database and they were averaged by each isotope's abundance in order to get each filter material's absorption cross-section, ultimately converted to transmission curves according to each sample thickness, element density and atomic molar mass. The details can be found in appendix A along with the transmission curve for each filters.

Table(1) presents, for both databases, the energy E_{res} that are removed by the first resonance in absorption of each filter. E_{exp} corresponds to the energy that should be used in the experiment to filter the second order harmonics ($E_{exp} = E_{res}/4$).

	EDNF database [15]			**In1 database**		
Filter	E_{res}(meV)	E_{exp} (meV)	$\frac{\sigma_{abs}(E_{res})}{\sigma_{abs}(E_{exp})}$	E_{res} (meV)	E_{exp} (meV)	$\frac{\sigma_{abs}(E_{res})}{\sigma_{abs}(E_{exp})}$
Hf	1058	264.5	56.28	1044	261	100
Er	441	110.25	17.53	456	114	10
In	1471	367.75	309.72	1456	364	333
Gd	2566	641.5	13.96	2600	650	20
Dy	1700	425	11.23	1733	433.25	15
Ir	641.6	160.4	26.79	-	-	-
Sm	874	214	2.49	-	-	-

Table 1: Filters' first absorption resonance

The absorption ratio $\frac{\sigma_{abs}(E_{res})}{\sigma_{abs}(E_{exp})}$ is a significant parameter, as it gives the absorption ratio between the energy that should be filtered and the experimental energy (E_i or E_f).

4.2 ALF Experiment : Method

The goal was to obtain experimental data on the transmission of each resonance filters. The experiment was carried out on ALF, a time of flight spectrometer of the ISIS pulsed neutron spallation source at the Rutherford Appleton Laboratory, UK. ISIS is a pulsed neutron source, and neutron energies are thus obtained from their time of flight. In this experimental set up of ALF, the total flight path length from the moderator to the monitor was 15.97 meters.

The samples consisted of thin foils of each filter element (with high purity: 99.9%, with 97% for Hf) placed on the direct beam path, and measured at room temperature. The filters available as samples had the following thicknesses d: Gadolinium 0.1 mm, Indium 0.1 mm, Iridium 0.1 mm, Cadmium 0.1 mm, Erbium 0.1 mm, Dys-

prosium 0.2 mm, Samarium 0.25 mm and Hafnium 0.25 mm.

To gain access to high energy neutrons, the nimonic chopper was dephased, and this allowed us to gather reliable data up to 10 eV. For statistical confidence, data was accumulated for each filter for a total integrated beam current around $70\mu Ahr$.

The acquisition method was the following : First, we measured the neutron count as a function of their time of flight for the empty beam without any filter on the path. The procedure was then repeated for each filter placed successively in the neutron beam path. By dividing in each case the spectrum with filter by the spectrum without filter, we obtained the transmission of each filter as a function of neutron time of flight t. For the Iridium sample, the beam size was reduced with a Boron diaphragm to accommodate the small sample size, and the empty beam spectrum was also measured with the diaphragm in place.

The time of flights were converted to energy (meV) using the following relation :

$$E = \frac{\hbar k^2}{2m_n} = \frac{h^2}{2m_n\lambda^2} = \frac{m_n}{2}v^2 = \frac{m_n}{2}\frac{L^2}{t^2} = 5.2276 \cdot 10^{-6}\frac{L^2}{t^2}$$

with L the flight path lenght in meter, and t the time of flight in seconds.

From this we obtained for each filter the transmission curve as a function of energy, sometimes also plotted as a function of wavenumber k.

4.3 Results : Transmission data from the ALF experiment

The measured transmission of each filter element for energies up to 10 eV are plotted in figure 6 as a function of the neutron wave-number. The observed abrupt reduction of transmission at particular k values are typical characteristics of neutron absorption resonances.

For comparison, the tabulated data obtained from the EDNF database [15] is also plotted on figure 6 (green curve). The agreement between the measurements and the database are very clear from the transmission curve, as both the position and the width of the absorption peaks are similar.

The absorption cross section for low energy neutron was also accessible in this dataset. Absorption cross-section at low energy neutrons usually increases linearly with λ, and is thus proportional to $1/k$. We checked that this relation holds for the filters studied, using the absorption cross section tabulated values (from [16]) for 2200 m/s neutrons (k=3.49 Å^{-1}).

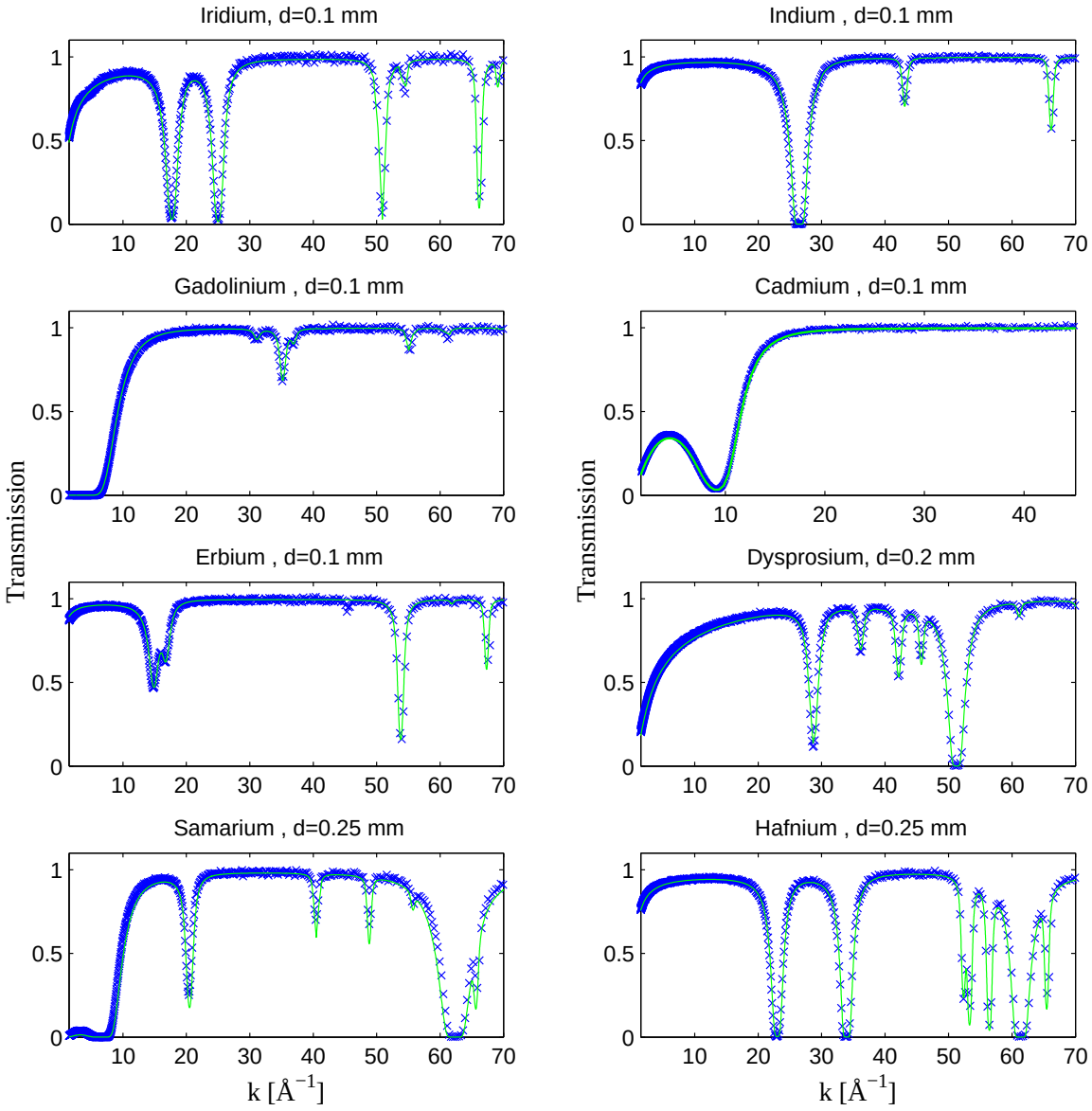

Figure 6: Transmission as a function of wavenumber for each resonance filter as measured on ALF (blue crosses), compared to the EDNF database resonance curve (solid green curve).

In the example of Dysprosium, the tabulated absorption cross-section for 2200 m/s neutrons is 994 barns so that $\sigma_{abs,Dy} = 3473/k$. As figure 9 shows, this is coherent with our dataset up to k=24.5 Å^{-1}, at which the first absorption resonance of the Dysprosium filter begins.

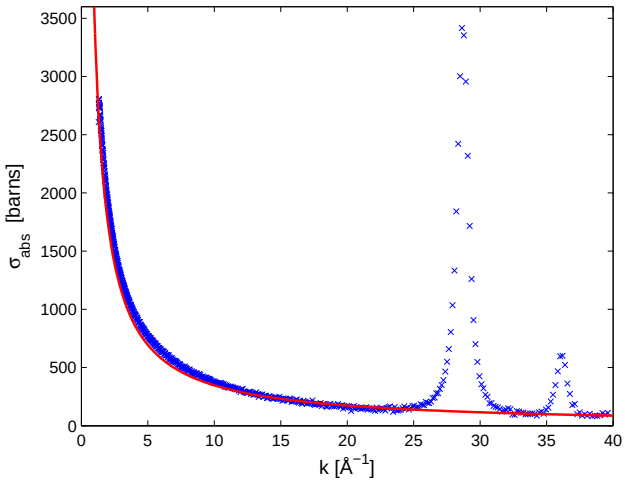

Figure 7: Absorption cross section of Dysprosium with ALF dataset (bue crosses) and fit of the absorption cross section for low energy neutrons (red solid curve)

Gadolinium, Samarium and Cadmium are the filters with the strongest thermal neutron absorption cross section (tabulated values respectively 49700 barns, 5922 barns and 2520 barns for 2200 m/s neutrons), making them efficient thermal neutron filters. This characteristic is visible on the transmission curves (Fig. 6), as low transmission values are reached at small wave-numbers (below 10 Å^{-1}). On the other hand, Iridium, Hafnium, Indium, and Erbium have low absorption cross section (tabulated values in [16] respectively 425, 104, 193 and 159 barns) for under 100 meV neutrons, so that large decreases in transmission only occur at the measured resonances.

4.4 Analysis of results

From our transmission data, the possibles uses for such absorption resonance filters were studied, with goal of designing a hot neutron experiment in which spurious signals can be removed based on the crucial experimental parameters : the incident and outgoing energy E_i and E_f, with the resulting energy transfer $\Delta E = E_i - E_f$.

In these experiments, spurious signal can come from either $\lambda/2$, the contamination from second order harmonics that arises when $Ef = Ei/4$, or from the incoherent scattering when the incident beam of energy E_i hits the analyser. Removal of the $\lambda/2$ contamination requires a filter with a resonance at energy of the second order harmonics, while a E_i notch filter removes the incoherent scattering. These filters uses are detailed below.

4.4.1 Use of a $\lambda/2$ Filter

The choice of a $\lambda/2$ filter requires knowledge of the characteristics of the absorption resonance peaks of each material. To remove the thickness dependency from the measured data, the transmission of each filter was converted to absorption cross section as a function of neutron energy.

The absorption resonance peaks were each fitted with Lorentzian functions :

$$f(E) = A\frac{\tau^2}{\tau^2 + (E - E_c)^2}$$

with τ the peak width and E_c the centre of the peak, which corresponds to the resonance energy.

Such analysis was only performed for all resonances up to 3 eV, as higher energy filtering is unlikely to be required, based on the accessible neutron spectrum of current neutron facilities. Indeed the neutron flux rapidly decreases with energy and the risk of second order contamination above 3 eV is very small.

Figure 8 shows that the fitted Lorentzian reproduce very closely the obtained absorption resonance peaks profiles. The characteristics of each absorption resonance peak (resonant energy, absorption ratio and full width at half maximum) could thus be extracted from the Lorentzian fit of the absorption peak.

Table 2 shows the results of this analysis by giving the absorption resonance energy value E_{res} for each filter, as well as the energy E_{exp} (1/4 of E_{res}), which corresponds to the particular energy one should work with in an experiment in a combination with such a filter.

The absorption ratio $\sigma_{abs}(E_{res})/\sigma_{abs}(E_{exp})$ is also included in table 2, and provides information on the efficiency of a filter. Indeed, a large ratio should be favoured in order to remove unwanted energies without a significant reduction of the intensity at the experimental energy.

In that respect, the Indium filter is the best, with a very high absorption ratio, followed by Hafnium with a ratio 2 folds lower. The low absorption ratio of the

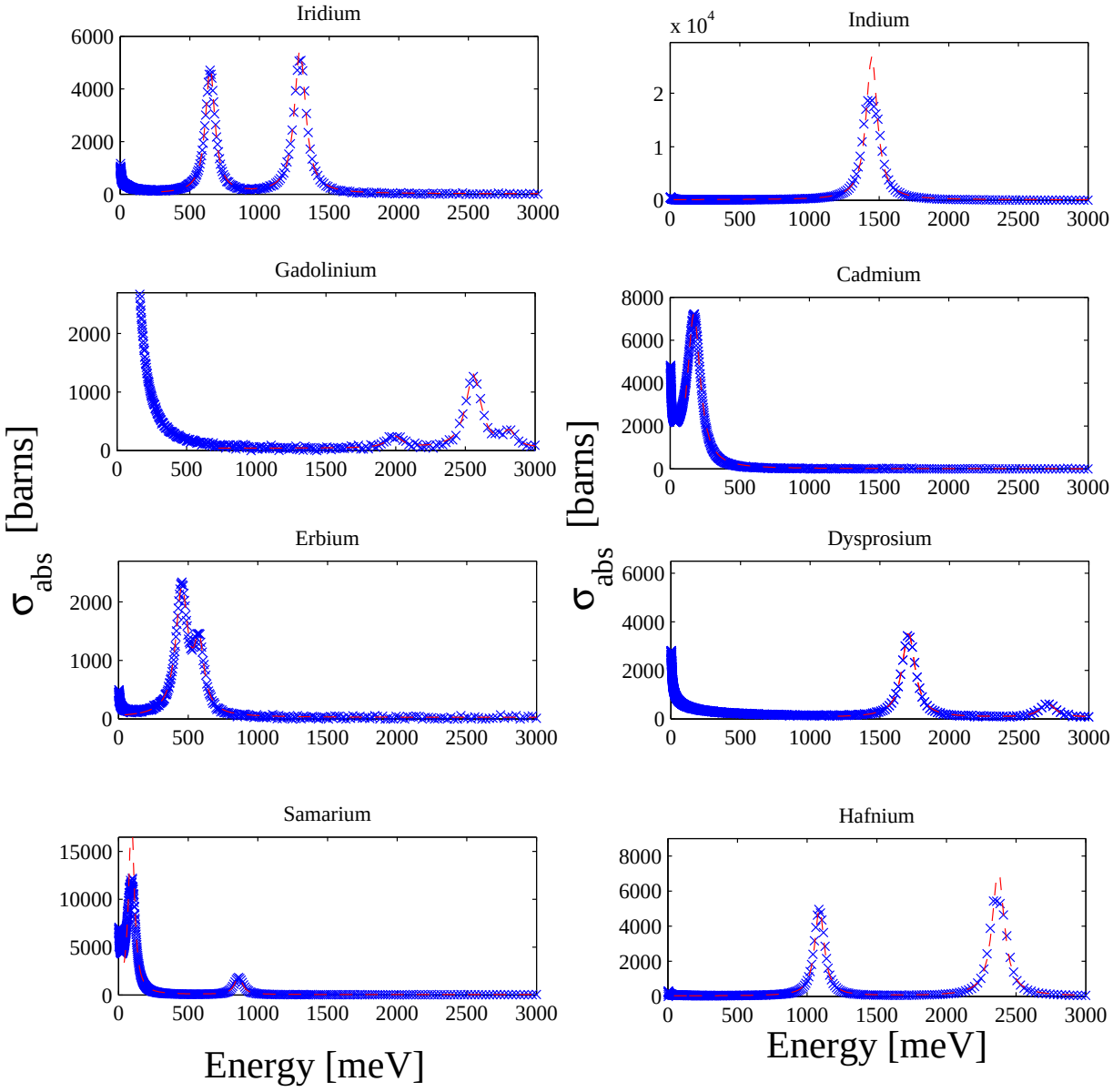

Figure 8: Absorption cross section as a function on neutron energy for each resonance filter measured on ALF (blue crosses), with Lorentzian fit of the absorption resonance peaks (dashed red curve).

Table 2: From ALF experiment : filters' absorption resonance energy E_{res} up to 3 eV, working wavelength $E_{exp} = E_{res}/4$, absorption ratio $\sigma_{abs}(E_{res})/\sigma_{abs}(E_{exp})$ and full width at half maximum FWHM.

Filter	E_{res}(meV)	E_{exp} (meV)	$\frac{\sigma_{abs}(E_{res})}{\sigma_{abs}(E_{exp})}$	FWHM (meV)
Sm	91	23	2.7	59
Sm	861	215	3.05	80
Cd	164	41	3.2	131
Er	454	113.5	16.4	126
Er	578	144.5	9.9	99
Ir	646	161.5	26.8	96
Ir	1291	323	36	113
Hf	1088	272	94.8	96
Hf	2371	593	96.7	120
In	1447	362	201	113
Dy	1706	426.5	14.6	132
Dy	2705	676	3.5	150
Gd	1991	498	1.2	149
Gd	2558	639.5	10.6	153
Gd	2815	704	3.9	88

resonances of Samarium (2.7 and 3) limits its use as a resonance filter. However, along with Cadmium and Gadolinium, its high absorption cross section at low neutron energies makes it a potential thermal neutron filter.

Erbium's first resonance also has a absorption ratio of 16.4, which means that it will be efficient as a filter only if its thickness is sufficient. We will see below how to optimize filter thickness.

Additional information on the selectivity of the filters can also be obtained from the full width at half maximum of the Lorentzian fits of the absorption peaks, allowing to choose an E_{exp} that is not exactly a fourth of the resonance energy.

4.4.2 Use of an E_i notch filter

To remove incoherent scattering, a notch filter with a resonance at E_i can be placed after the sample. The available experimental energy transfer range then depends on the transmission of the filter below E_i. The choice of a particular notch filter must then take to account the energy at which thermal neutron absorption becomes dominant, and the width of the absorption resonances.

In case of Iridium, the resonance corresponding to $E_i = 646$ meV can be used to suppress incoherent scattering. For an reduction of E_i by a factor 10, the range of E_f with a transmission above 80% is [21,511] meV, so that this particular filtering can be used for energy transfer higher than 135 meV. For a reduction of E_i by a factor 100, the range of E_f with a transmission above 80% is reduced to [81,427] meV, so that it is suited for energy transfer from 219 meV up to 565 meV. In the case of Iridium, the thermal absorption cross section is sufficiently low to allow very high energy transfer.

However, in the case of Dysprosium or Gadolinium, for example, their high thermal absorption ratio would limit the available energy transfer when they are used as a notch filter. Filter can thus be chosen as notch filter, though the limit on the range of energy transfer it implies must be considered using the transmission data.

4.4.3 Thickness optimization

To optimize the choice and use of a particular filter, further insight can be obtained based on the thickness dependency of the filter transmission T, where $T = e^{-\mu d}$, with d the thickness of the material and μ the linear absorption coefficient.

μ is proportional to the absorption cross section σ_{abs} : $\mu = \rho N_a \sigma_{abs}/M$, with ρ the element density and M its atomic molar mass. Adjustment of the thickness thus

allows optimisation of the filtering efficiency.

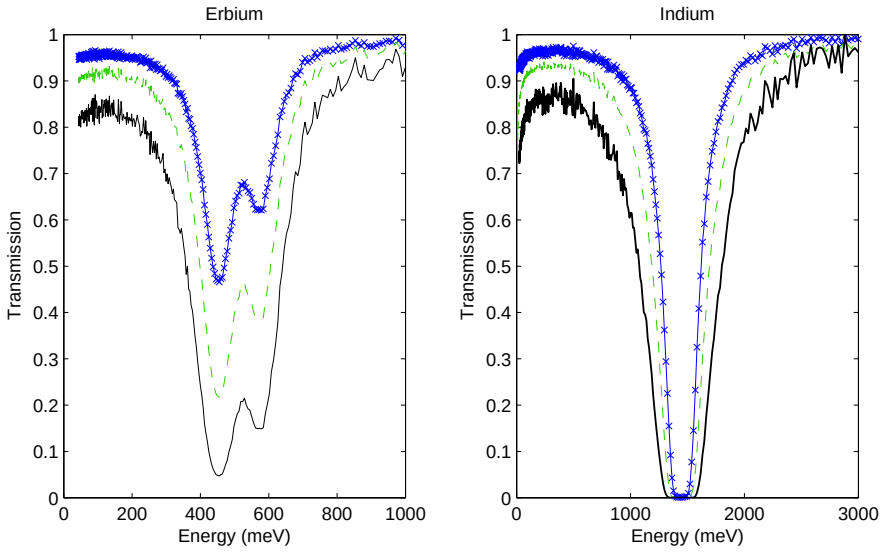

Figure 9: Transmission of Erbium (left) and Indium (right), for a filter thickness of 0.1 mm (blue crosses), 0.2 mm (green dashed curve) and 0.4 mm (black solid curve) in the energy range of their first absorption resonance. peak

As mentioned before, Erbium is a typical case where thickness optimisation is needed, as the absorption ratio $\sigma_{abs}(E_{res})/\sigma_{abs}(E_{exp})$ of the 454 meV resonance is low. With an Erbium filter of 0.1 mm thickness, the transmission at this resonance (the strongest of the double absorption peak) is just below 50%, with a transmission of 95% at E_{exp} (figure 9).

By doubling the thickness of such a filter, the transmission at the resonance is reduced by 53% ($T = 0.21$ when E=454 meV) while causing only a 4% reduction of the signal intensity at E_{exp}. In order to obtain almost complete filtering at the resonance, a Erbium filter of 0.04 mm can be used to reduce the transmission at the resonance to 4.7% while causing a mild reduction of the intensity at E_{exp} with a transmission lowered to 89%.

A further effect of increasing the thickness is the broadening of the absorption resonance, which can be desirable in order to filter out energies away from the resonance energies. Indium's very high absorption ratio, which reduces transmission at the resonance to zero with a filter of 0.1 mm, allows this material to demonstrate the effect. Upon the increase of the filter thickness, the absorption resonance peak broadens

(fig. 9) and in the case of Indium, a filter of 0.4 mm instead of 0.1 mm increases the full width at half maximum of the resonance peak by 105%, while causing only a 9% reduction of transmission at E_{exp}.

5 La_2CuO_4 experiment on In1 spectrometer

5.1 Experimental preparation

As the goal of the experiment was to observe the anomaly at the $(\pi, 0)$ point, where the excitation energy is about 320 meV, the technical difficulty of this experiment lies in the high energy transfer that needs to be reached. Indeed, in order to obtain sufficient information on the spin excitation anomaly (around 320 meV), the aim should be to have access to energy transfers up to 350 meV. To optimize the choice of the experimental parameters such as E_i and E_f, a number of significant limitations must be considered.

Indeed, not any Q vector can be reached for a energy transfer of 320 meV, as there is a lower limitation on the 2θ angle of the scattering triangle (angle between k_i and k_f). If one uses a large tail vacuum tank, the lower limit on the 2θ angle can be estimated to be of 10 degrees.

A rough calculation with an E_f fixed to 360 meV, an energy transfer of 350 meV, and $2\theta = 10$ yields a minimum $|Q|$ vector of 5.98 Å. This means that, for each possible configuration, there exists a minimum Q vector.

The energy scan should be done at an equivalent of $Q = (\pi, 0)$ ($|Q| = 0.819$ Å^{-1}) and $Q = (\pi, \pi)$ ($|Q| = 0.579$ Å^{-1}). One thus needs to go to higher Brillouin zones to increase $|Q|$. Equivalent multiples of $Q = (\pi, 0)$ are $(a \cdot \pi, b \cdot 2\pi)$ with $a \neq 0$ odd and b even.

However, this brings about a second crucial limitation, the magnetic form factor of the Cu^{2+} orbital which drops when $|Q|$ goes up. Going to higher incident energy E_i conveniently decreases $|Q|$, but the neutron flux also decreases and resolution worsens, and this must be taken into account.

Finally, one should avoid spurious signal and background from noise. The large tail vacuum tank can improve this by preventing air scattering, and choosing one of the absorption resonance filters studied can help in removing spurious signals.

This chapter details the study that led to these choices in terms of possible filters and their associated choice of energy, Q vector, and range of scattering angles.

5.1.1 Cu^{2+} Magnetic form factor

The minimum Q for a minimum 2θ of 10 degree is dependent on E_i and E_f, and for an hot neutron triple axis where E_i can be as high as 700-800 meV, $|Q|_{min}$ can be roughly estimated as higher than 5.5 Å^{-1}.

For the Cu^{2+} ions of La_2CuO_4 , we must consider the $d_{x^2-y^2}$ orbital, which leads to an anisotropic magnetic form factor, thus dependent on the direction of the wave vector q (parallel or perpendicular to z). In our case we are interested in the case $q \perp z$. However the angle averaged form factor squared and the $q \perp z$ anisotropic form factor squared are very similar so that one can use in this case the analytical form factor calculated from the international tables for crystallography[17].

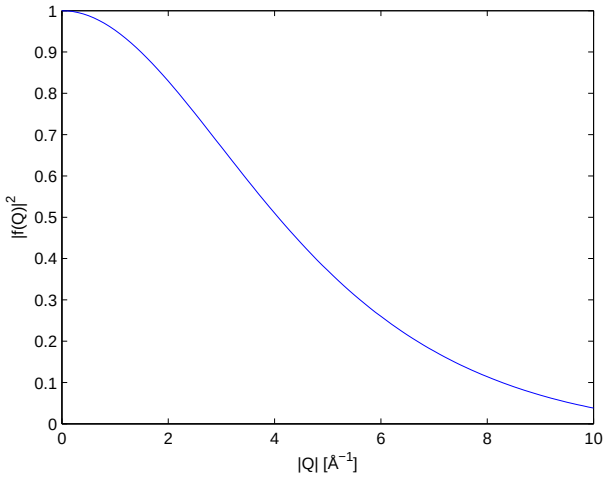

Figure 10: Magnetic form factor squared $|F(|Q|)|^2$ for the $d_{x^2-y^2}$ orbital of Cu^{2+}

From the steep decrease of the magnetic form factor with $|Q|$, it is obvious that $|Q|$ should be kept to the lowest value possible with regards to the high incident energy limitations.

5.1.2 Choice of Monochromator

In order to reach high incident energy on a hot neutron spectrometer, a Cu(331) monochromator was chosen. It allows an E_i up to 800 meV, with the expected decrease in flux as E_i increases (fig. 11).

Reaching a compromise between the need for small $|Q|$ and the flux at large E_i was needed in order to optimize the magnetic scattering cross-section. The magnetic

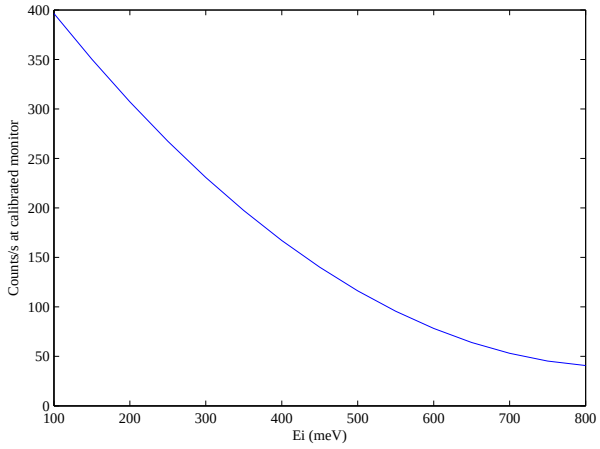

Figure 11: Flux as a function of E_i for the Cu(331) monochromator of IN1 (smoothed curve from IN1 database)

form factor was combined with the Cu(331) monochromator flux, giving an estimate of the optimal incident energy choices for an energy transfer of 350 meV (figure 12).

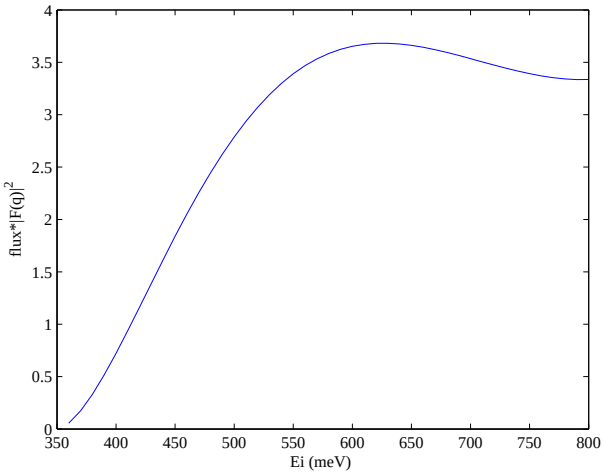

Figure 12: $Flux \cdot |F(q)|^2$ as a function of E_i for the Cu(331) monochromator for an energy transfer of 350 meV and $2\theta = 10$

Based on this, the appropriate range of energies E_i would be between 550 to 700 meV, so that the chosen filter should be fitted to an incident energy in this range.

5.1.3 Filter selection

Available filters for the experiments are the same thin foils as studied in section 4.4.1, namely Hafnium, Erbium, Indium, Iridium, Gadolinium, Dysprosium, Cadmium and Samarium. One of these filters can be used to filter out the second harmonics of the incident or outgoing beam, which means that the chosen filter should have an resonance peak in absorption cross-section at 4 times the desired experimental energy.

Based on the absorption resonance table (table 2) in the section 4.4.1, one can thus choose among a few possibilities. The planned interval of energy transfer is [0,350] (meV).

First of all, an Indium filter (placed after the sample) presents the advantage of a large absorption ratio of about 333. Such a choice would lead to a fixed $E_f = E_{exp} = 364$ meV. Thus the incident energy E_i would vary in the interval [364,714] (meV), with 714 meV in the optimal part of the $Flux \cdot |F(q)|^2$ curve (Fig. 13). However, second order filtering is unlikely to be needed as the flux at such high energy is very low.

Another possibility would be Hafnium (placed after the sample), which leads to a fixed $E_f = E_{exp} = 261$ meV. E_i would thus be in the interval [261,611], at lower energies than In filter, which might improve the resolution. However the absorption ratio is 6 folds lower, and as with Indium the need for such a filter is limited.

Iridium could also be used as a filter, with an absorption ratio of about 26, allowing the use of a thin 0.1 or 0.2 mm foil. Iridium filter would be placed after the sample, with a fixed $E_i = 161$ meV. Therefore E_i would be in the range [161,511]. This would allow to keep E_i low while being close to the optimal energy region.

The last filter considered is Erbium, with a fixed $E_f = E_{exp} = 114$ meV. This leads to an E_i in the interval [114,464]. However, this means that at a 350 meV energy transfer, E_i is only 464 meV which is not quite in the optimum of the $Flux \cdot |F(q)|^2$ curve (13). The absorption ratio is lower than Iridium, so that thicker foil might be needed. Nevertheless, this possibility will be explored as Erbium is a commonly used filter on In1, and it might be useful if the resolution gets too bad with higher incident energies.

Figure 13 visually summarizes these choices.

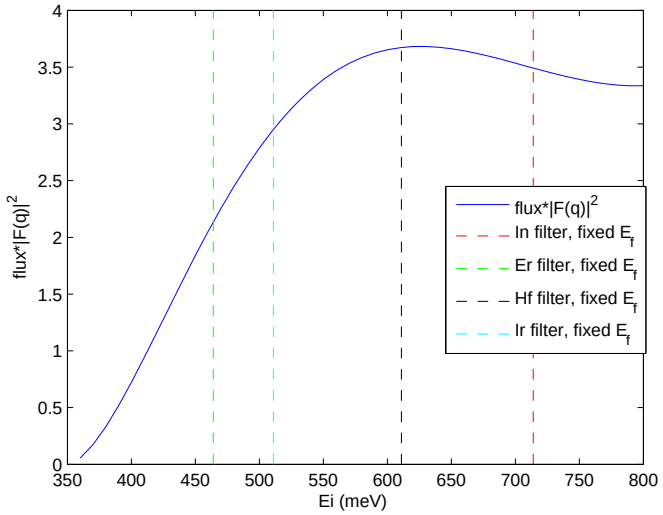

Figure 13: $Flux \cdot |F(q)|^2$ as a function of E_i for the Cu(331) monochromator for an energy transfer of 350 meV and $2\theta = 10$, with filter choices

5.1.4 Analyser

The reflectivity of the analyser should also be taken into account. From figure 14, it can be seen that there are values of E_f for which the reflectivity is significantly lower than others.

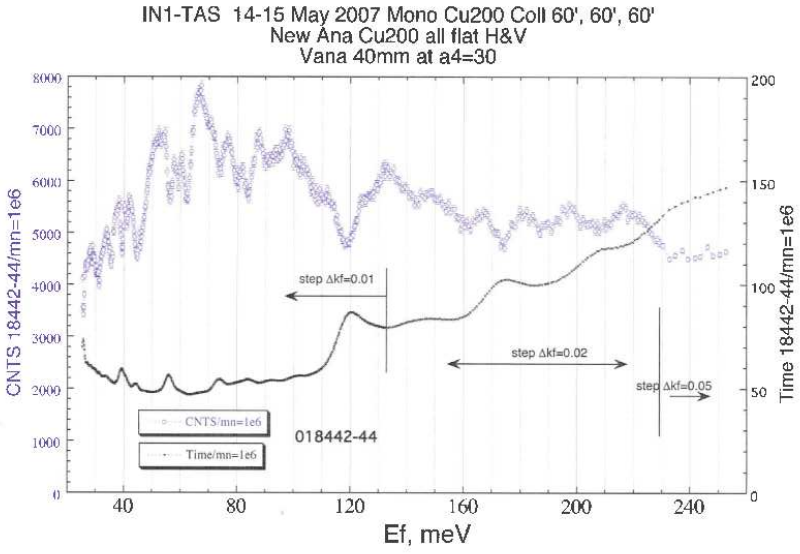

Figure 14: Reflectivity of the Cu(200) analyser as a function of E_f, from IN1 database

This should be taken into account when measuring at fixed E_f. If the absorption resonance peak of the chosen filter is broad enough, one could still filter the second harmonics while slightly shifting the E_f to avoid the dip in reflectivity.

5.1.5 Range of scattering angles

The table 3 shows the range of scattering angle 2θ that will allow an energy transfer in the interval [0,350] meV at an equivalent of $Q = (\pi, 0)$ and $Q = (\pi, \pi)$ for the four filters mentioned above. For the present experiment however, only Erbium and Iridium filtering were planned.

In filter $\lvert Q\rvert_{min}$=5.97 Å^{-1}			Hf filter $\lvert Q\rvert_{min}$=6.42 Å^{-1}		
Q vector	$\lvert Q\rvert$	2θ range	Q vector	$\lvert Q\rvert$	2θ range
$(7\pi, 2\pi)$	5.96	[9.69,26.0]	$(7\pi, 4\pi)$	6.6	[11.9,34.3]
$(7\pi, 4\pi)$	6.6	[14.4,28.8]	$(11\pi, 11\pi)$	6.37	[9.5,33.0]
$(11\pi, 11\pi)$	6.37	[12.9,27.8]	$(13\pi, 11\pi)$	6.97	[15.1,36.2]
Er filter $\lvert Q\rvert_{min}$=7.76 Å^{-1}			Ir filter $\lvert Q\rvert_{min}$=7.18 Å^{-1}		
Q vector	$\lvert Q\rvert$	2θ range	Q vector	$\lvert Q\rvert$	2θ range
$(9\pi, 4\pi)$	8.07	[15.6,65.9]	$(9\pi, 0)$	7.37	[12.9,49.5]
$(13\pi, 15\pi)$	8.13	[16.6,66.5]	$(13\pi, 13\pi)$	7.53	[14.9,50.6]

Table 3: Range of scattering angles for each possible Q vector with energies defined by the filters (Indium, Hafnium, Erbium, Iridium)

5.2 Chosen experimental method

The preliminary method had the following steps :

- Orientation of the crystal using the structural Bragg peaks at Q=(200) and Q=(020).
- Mapping of the magnetic Bragg peaks of the wanted Brillouin zone in order to get a map of the resolution ellipsoid, particularly in (Q_k, Q_h) plane and in terms of energy.
- Transverse and longitudinal scans at 100 meV energy transfer to see the spin wave excitations around (π, π) point.
- Scanning up at the (π, π) point from 0 energy transfer to 320 meV.
- Energy scans at the $(\pi, 0)$ equivalent point from 300 to 350 meV in order to scan in the region of the anomaly.

5.3 In1 set-up

The In1 spectrometer was in the W configuration (figure 15), with a Cu331 monochromator to maximize the flux at high incident energy, and a Cu200 analyser to select the desired E_f . The collimators were set to the "open" configuration in order to maximize the neutron flux at high energies.

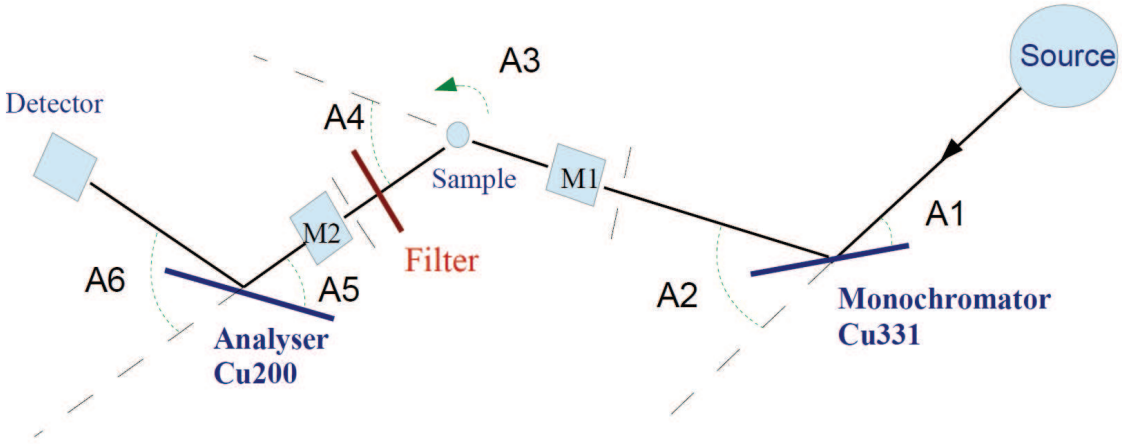

Figure 15: schematic drawing of the chosen configuration of the In1 spectrometer: with A1-A6 the configuration angles of the instrument and M1 an M2 the monitors

The La_2CuO_4 sample (5.2 g) was mounted on its sample holder with the reciprocal axis a* and b* in the scattering plane (figure 16). The sample was placed in a cryostat with a large diameter vacuum box (110 cm) in order to limit air scattering at low scattering angles. The La_2CuO_4 sample was cooled to 2.5 K.

Figure 16: La_2CuO_4 sample mounted on sample holder, after adjustement of the alignement on IN3

Two energies E_f corresponding to the Iridium and Erbium filters were ultimately selected in this experiment, leading to k_f values of respectively 9 and 7.5 $Å^{-1}$. The filters were placed after the sample, before the slits and monitor 2 (fig 15). With each change of the wave-number, the focusing had to be adjusted in terms of the translation of the analyser (-10 for k_f=7.5 and -5 for k_f=9), the vertical analsyser curvature (10.6 and 13) and the horizontal analyser curvature (5 and 4.5).

Using Rescal matlab program to get the resolution ellipsoid with the Cooper-Nathan's method ([18]), we estimated the expected energy resolution at the equivalent $(\pi, 0)$ point for 300 meV energy transfer in both fixed k_f cases. In the $k_f = 7.5$ case, the accessible point is $(9\pi, 4\pi)$, and the energy resolution is approximately 34 meV. Similarly for the $k_f = 9$ case, where $Q = (9\pi, 0)$ is accessible, it is of 41 meV. This is similar to the energy resolution obtained for the intensity peak of reference [5]. We notice that the resolution worsens only slightly when shifting to a higher k_f as it allows the choice of a shorter Q vector.

5.4 Results

Out of the total planned beam-time, only half could be used for the experiment due to mechanical difficulties with the monochromator angles, which means that a further experiment will be performed to see the anomaly in a future ILL reactor cycle.

Presented here are the results of the scans that were performed during the experiment. In figure 17 are presented the equivalent Q points of the brillouin zone that were reached in the experiment. $(\pi, 0)$ is the Q vector at which we expect to see the anomaly at 320 meV, (π, π) corresponds to the magnetic Bragg peak, $(\pi/2, \pi/2)$ is a saddle point where an A3 scan follows a constant energy contour ,and $(2\pi, 2\pi)$ allows background measurements as it is a point where there should be no magnetic excitations.

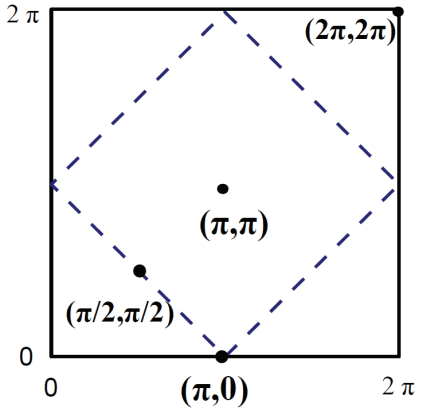

Figure 17: La_2CuO_4 Brillouin zone with equivalent points reached in the experiment

5.4.1 Effect of mosaicity on resolution

The problem we faced in this experiment is that the La_2CuO_4 crystal was twinned and thus had a large mosaicity. From figure 18(a), we can see that there is a mosaicity of approximately 7 degrees, as we see 3 different Bragg peaks in the A3 scan done at the $Q = (200)$ structural Bragg peak.

The presence of the three peaks was also checked at $k_f = 9$ Å^{-1}, with and without the Iridium filter which confirmed that this was due to the presence of several crystallites in the sample and did not correspond to any spurious signal. The

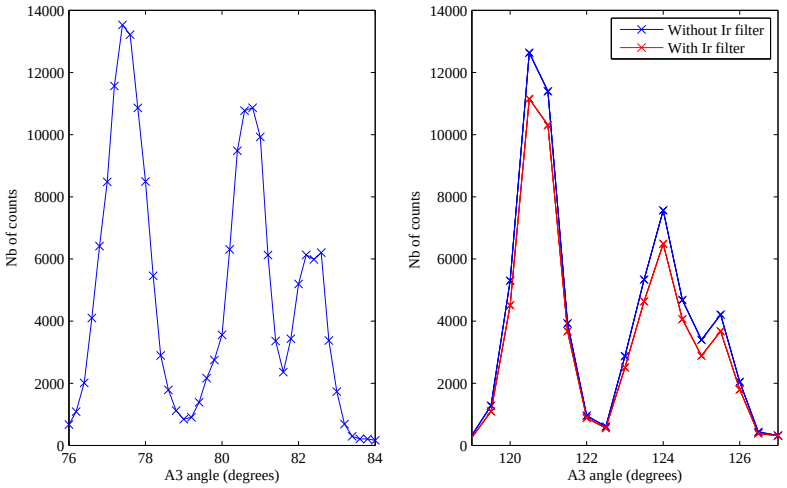

(a) A3 scan of the 200 nuclear bragg peak with respectively k_f =7.5 Å^{-1}(left) and k_f = 9 Å^{-1}(right)

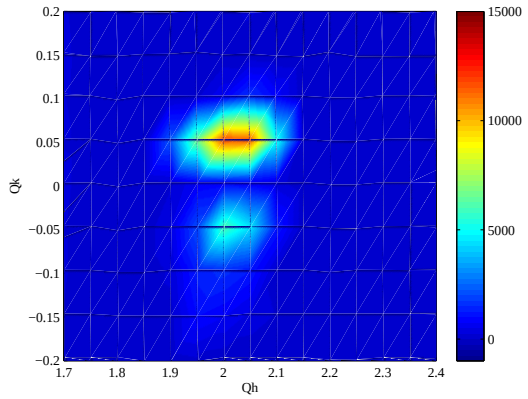

(b) Map of 200 nuclear bragg peak with Ir filter and k_f =9 Å^{-1}

Figure 18: A3 scan of the La_2CuO_4 sample at the (200) Bragg peak, showing mosaicity

spatial resolution in Q space can also be seen on figure 18(b), where the different crystal domains are again visible.
One of the consequence of such a large mosaicity is that the energy resolution worsens. Using again Rescal, but with the mosaicity taken into account (ETAS is now set to

420, corresponding to 7 degrees sample mosaicity), the energy resolution for a $(\pi, 0)$ point at 300 meV energy transfer becomes : 71 meV for $k_f = 7.5$ Å^{-1}, and 108 meV for $k_f = 9$ Å^{-1}and thus any peak in this range will be very broad.

5.4.2 Scan at (π, π) magnetic Bragg peak equivalent

Due to the mosaicity, $k_f = 9$ and $k_f = 7.5$ have much worse resolution than expected, and so, at the large energy transfer we want to reach, $k_f = 9$ will probably not yield any interpretable data .

Therefore, only shown here are the scans for $k_f = 7.5$ in the $(10\pi, 0)$ Brillouin zone. Not presented here are the performed scans that allowed the choice of the best k_f and equivalent point of the Brillouin zone based on the resolution maps of the magnetic Bragg peaks. To reach 300 meV transfer and to avoid direct beam by keeping a large enough A4 angle($A4 > 14$ degrees to be safe), with $k_f = 7.5$ Å^{-1}, one has to go to the Brillouin zone with $(10\pi, 0)$ as a equivalent to $(0, 0)$.

At the position fo the expected magnetic Bragg peak $(11\pi, \pi)$, the observed peak (fig. 19(a)) was displaced in Q space, probably due to the crystallites, with the magnetic peak centred on $Q = (5.4, 0.35, 0)$ instead of $Q = (5.5, 0.5, 0)$. Centering on the displaced magnetic peak position, a Q_h scan (best resolution with a longitudinal scan) was performed at zero energy transfer (figure 19(b)).

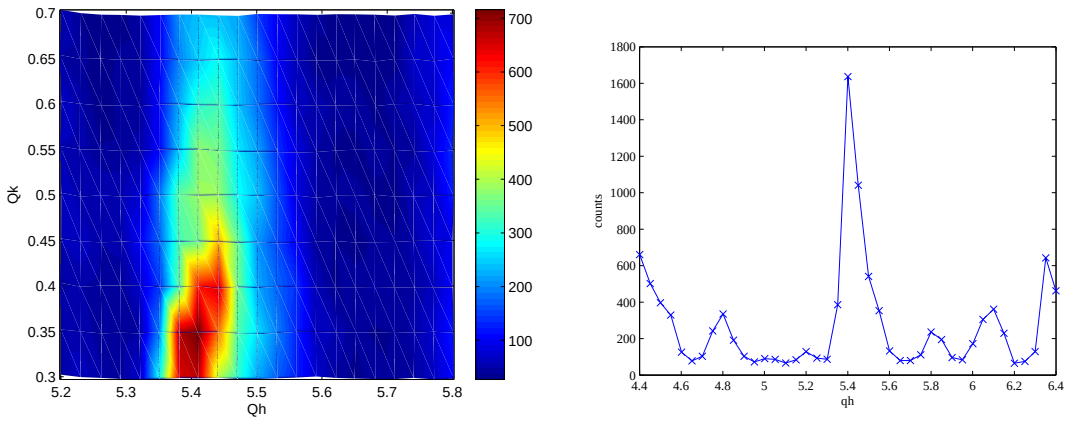

(a) Map of $(11\pi, \pi)$ magnetic bragg peak with $k_f = 7.5$ Å^{-1}

(b) Qh scan at 0 energy transfer near $(11\pi, \pi)$ magnetic bragg peak with $k_f = 7.5$ Å^{-1}

Figure 19: $Q = (11\pi, \pi)$ magnetic Bragg peak at 0 energy transfer

A Q_h scan for 50 meV energy transfer was then done (Figure 20). However, there is a lot of visible spurious signal and the expected peak, though visible, cannot be clearly separated from the background, probably due to the poor resolution resulting from the mosaicity of the sample. A further scan was done at 100 meV energy transfer, but no identifiable peak was visible amidst the background signal.

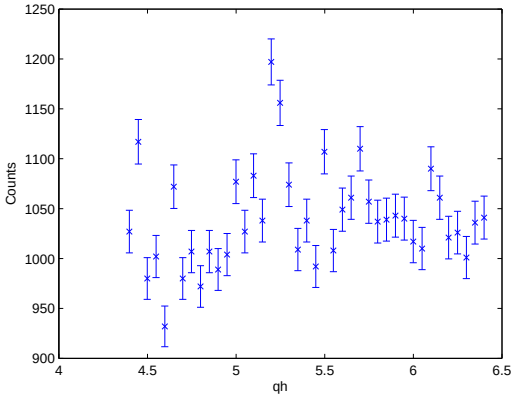

Figure 20: Qh scan at 50 meV energy transfer near $(11\pi, \pi)$ magnetic bragg peak with $k_f = 7.5$ Å^{-1}

5.4.3 Scan at $(\pi/2, \pi/2)$ and measured background

As mentionned previously, $(\pi/2, \pi/2)$ is a saddle point of the Brillouin zone, where performing an A3 scan corresponds to following a constant energy contour.

This makes it a point of interest in our case as the mosaicity should not have such a large impact on the measured excitations at $(\pi/2, \pi/2)$. Indeed, when performing an energy scan (with $k_f = 7.5$) at the $(\pi/2, \pi/2)$ equivalent point of the Brillouin zone of interest $(10.5\pi, 0.5\pi)$, all crystallites should contribute to the intensity of the magnetic excitation.

For $Q = (10.5\pi, 0.5\pi)$, we would expect a peak around 280 mev according to the spin wave dispersion (fig. 4), and a background signal at other energies. The result of the energy scan with $\hbar\omega$ in the range [220:360] meV is shown in figure 21, for a counting time of approximatly 6 minutes (time is dependant on monitor count M1).

The expected 280 meV peak is visible, but there is also one very strong peak at 340 meV that should corresponds to a spurious signal, as not peak is to be expected

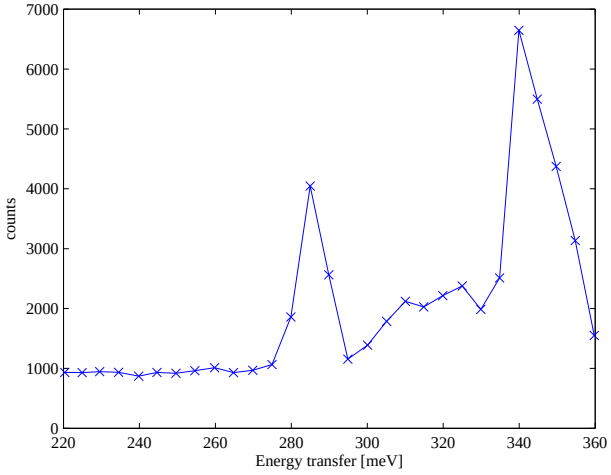

Figure 21: Energy scan at $Q = (10.5\pi, 0.5\pi)$, $k_f = 7.5$ Å^{-1}

at this energy transfer.

In order to confirm that it corresponds to a spurious signal, the same energy scan was performed at a point where no magnetic excitations is expected from spin wave theory : an equivalent of $(2\pi, 2\pi)$, which here corresponds to Q=$(10\pi, 0)$. This will allow a measurement of the background signal (figure 22) that can then be compared to the $Q = (10.5\pi, 0.5\pi)$ scan .

The energy scan shows that the strong peak at 340 meV is still present, and that placing a 0.2 mm thick Erbium filter after the sample reduces its intensity by 80%. With an energy transfer of 340 meV, and $E_f = 114$ meV, this means that at this point E_i was 454 meV, which corresponds to the absorption resonance of the Erbium filter (from table 2). In addition the reduction of the intensity corresponds to the expected transmission at the resonance energy with this thickness (in section 4.4.3). This means that here Erbium acts as a notch filter (described in 4.4.2) which removes the incoherent scattering that led to the spurion at 340 meV.

5.4.4 Scan at $(\pi, 0)$ equivalent

Even though the mosaicity of the crystal prevents reliable data to be gathered at the $(\pi, 0)$, an energy scan at the Q where the anomaly has been observed was performed, in order to allow comparison with the future follow-up measurements.

In the considered Brillouin zone, $(\pi, 0)$ corresponds to $(11\pi, 0)$, and the energy

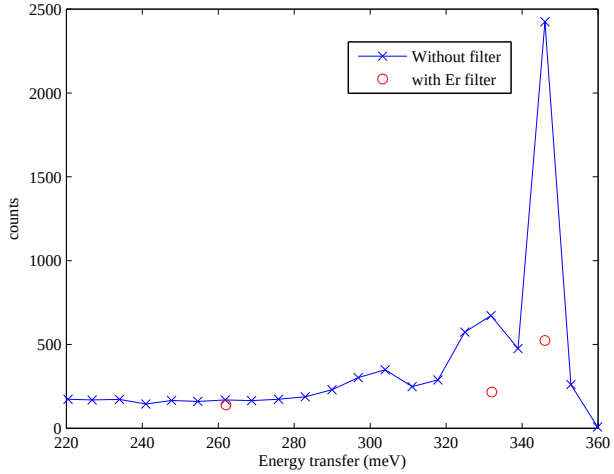

Figure 22: Energy scan at $Q = (10\pi, 0)$, $k_f = 7.5$ Å^{-1}

scan was realised with about 18mn per points (again the time per point was fixed by monitor counts M1). The result of the scan is shown in figure 23.

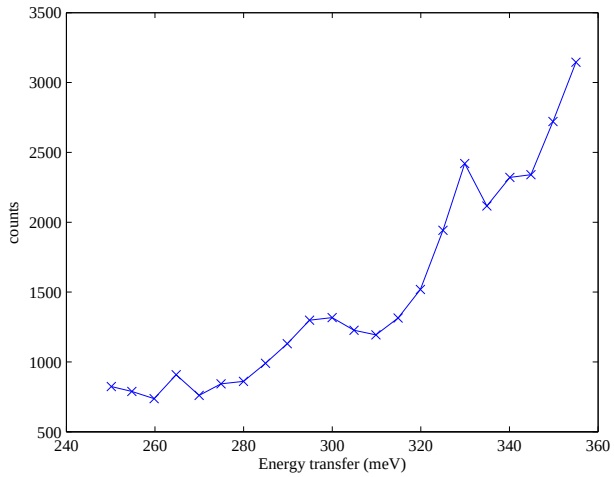

Figure 23: Energy scan at $Q = (11\pi, 0)$, $k_f = 7.5$ Å^{-1}

It is difficult to distinguish in the obtained scan between what corresponds to background and spurious signal, what can be a consequence of mosaicity and thus we cannot extract from the scan the intensity accounted as the profile of the magnetic

excitation. Nevertheless a peak seems to start at 320 meV, though the peak intensity increases continuously. In addition, as the A4 angle (i.e. 2θ) decreases as energy transfer increases, so it could also be that the direct beam starts to be detected.

5.5 Follow up of experiment

As the available beam time was reduced to half of the planed beam time, further scans can be planned for the rest of the beam time based on the analysis of the presented results.

Although the spurious signal observed at $\hbar\omega = 340$ meV can be removed by the Er filter, it might be best suited to work at $k_f = 9$ in order to avoid incoherent scattering with an energy so close to the energy region of interest where we hope to see the anomaly. However this requires a crystal with a lower mosaicity. If an untwinned crystal can be obtained (which is not an easy task for La_2CuO_4 as it is generally twinned due to the similarity of the orthorhombic axis a and b), one can then hope to optimise the signal to noise ratio for $k_f = 9$.

It also seems that scans of about 20mn per point give reasonable signal to noise ratio, although this will have to be adapted depending on the size of the used crystal, giving a approximate total time of seven hours for 21 points of an energy scan aiming to detect the $(\pi, 0)$ anomaly.

In addition, a similar scan to the energy scan at $Q = (11\pi, 0)$ with $k_f = 7.5$ should also be performed with a crystal with a smaller mosaicity, first without and then with the Erbium filter. This would possibly allow, by comparison with the scan presented in 5.4.4, to distinguish the magnetic excitation peak from background and spurious signal. In this case, and with a careful computation of the resolution function, the extracted signal from the scan would allow to reconstruct the line shape of the excitation at $Q = (\pi, 0)$.

6 CFTD Rita-II experiment

As discussed in 2.2.1, CFTD compounds are realisation of spin 1/2 square lattice Heisenberg Antiferromagnet. However, in the model 's nearest neighbour Heisenberg Hamiltonian, the anisotropy of the nearest neighbour interaction is not taken into account. It has been observed that there is an energy gap at base temperature, which implies that the anisotropy of J plays a significant role in magnetic excitations.

N. Christensen and an experimental team performed an experiment with a CFTD sample on the Rita-II instrument. Rita-II is a triple axis spectrometer for cold neutrons at SINQ, at the Paul Scherrer Institute (CH). The instrument was in the imaging mode, and E_f was set to 3.7 meV. The data from this experiment was used in this study to extract the anisotropy coefficients, with the help of theoretical calculations done by J. Jensen using the random phase approximation (RPA equations from [19]).

6.1 Spin waves with anisotropic exchange interaction

When considering only nearest neighbour interaction and assuming anisotropic exchange interaction, the Hamiltonian for CFTD as a 2D spin half system becomes :

$$H = \frac{1}{2}\sum_{ij}^{n.n.}\sum_{\alpha=x,y,z} J_\alpha S_\alpha(i) S_\alpha(j)$$

Assuming the ground state to be the Néel state with moments along the z axis, the excitation spectrum was derived by Jens Jensen in [20].
Due to the anisotropy, there are no Goldstone modes, and thus energy gaps are expected. From the calculations, the final susceptibility tensor is diagonal with two elements, and the excitation energies are :

$$E_\pm^2(\mathbf{q}) = 16\langle Sz\rangle^2[(J_z^2 - J_xJ_y) \pm J_z(J_y - J_x)\gamma_q + J_xJ_y(1-\gamma_q^2)]$$

with $\gamma_q = \frac{1}{2}[cos(q_1+q_2)a/2 + cos)q_1 - q_2)a/2]$

For $\mathbf{q} = (1,0,0)$ or $\mathbf{q} = (0,1,0)$, we have $\gamma_q = -1$ and these calculations predict two spin waves modes : a xx polarized mode and a yy polarized mode.

This model will be confronted to the Rita-II experiment in order to extract the anisotropy coefficients.

6.2 Experimental characteristics

The sample was oriented with the 2D-planes in the horizontal scattering planes. This allowed measurements of magnon dispersion along a* or b* (with Q transfer of $Q = (100)$ or $Q = (010)$), both of which correspond to $Q_{2D} = (\pi, \pi)$ in the 2D reciprocal space of CFTD [3].

At base temperature, the moments in CFTD compounds are ordered approximately along a*, so that the two spin waves modes are polarized along both perpendicular directions b* and c*.

The experiment was carried at several temperatures ranging from 1.6 K to 20 K and around momentum transfer Q=(100) and Q=(010). The energy scans were performed from an energy transfer of 0 to 5 meV.
Neutrons allow probing of spin components perpendicular to momentum transfer, so that at Q=(100), and at the lowest temperature, one can see spin waves polarized along both b* and c*. However at Q=(010), one can only observe spin waves polarized along c*, so that the peak intensity should be roughly divided by a factor 2 (assuming that the two polarization modes had equal intensity, which we will see is not quite the case).
Above $T_n = 16.54$ K, paramagnetic spins are expected, and all directions should be equivalent.

6.3 Extraction of anisotropy coefficients

In order to calculate the anisotropy coefficients, the energy of each gap from the base temperature scans are extracted. In this experiment, the lowest temperature energy scans were performed at $1.6K$ for both Q=(100) and Q=(010).

For the two $1.6K$ energy scans, each measured excitation peak was fitted with $I(E)$, which corresponds to half a Gaussian on the left of the peak (small energies) and half a Lorentzian at the right of the peak (higher energies) :

$$I(E) = \begin{cases} A_1 \exp(-\frac{(E-c)^2}{2\sigma^2}) & \text{for } E < c \\ A_2 \frac{\tau^2}{\tau^2+(E-c)^2} & \text{for } E > c \end{cases}$$

In the case of the Q=(010), only the c* polarised mode is visible (E_{yy} in the spin wave calculations) so that there is only one peak. The result of the fit is shown in figure 24, where one can see that it agrees well with the measured data. This

allows to fix E_{yy} to 0.52 for the second fit in order to reduce the number of varying parameters.

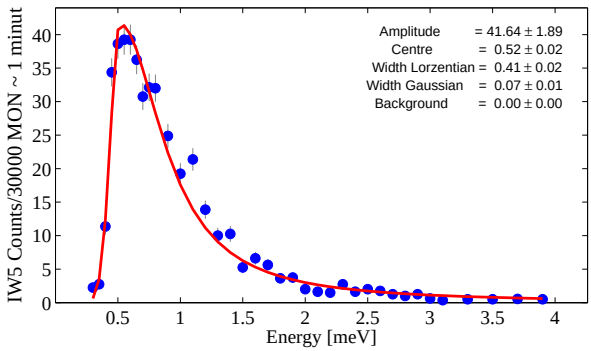

Figure 24: Energy scan for Q=(010) with fit function

Using the fit of the first energy gap, two I(E) functions are then used to fit the data measured for Q=(100), where both b* and c* polarisations are visible. Figure 25 shows the fitted data, where the plateau around 0.30 meV is reproduced.

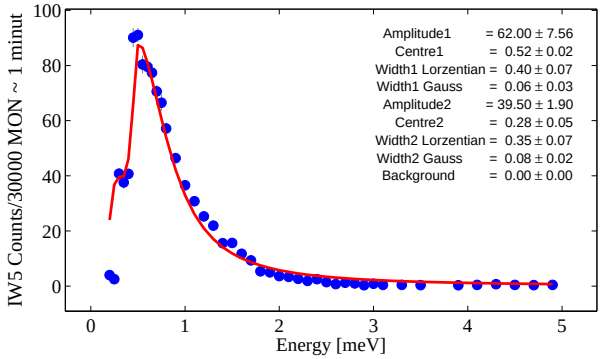

Figure 25: Energy scan for Q=(100) with fit function

Based on the fits, the excitation energies are estimated to be $E_{xx} = 0.28 \pm 0.05$ meV and $E_{yy} = 0.52 \pm 0.02$ meV.

From this, the anisotropic exchange interaction coefficients $J_z = J$, J_x and J_y can be estimated.

Let $J_z = J$ $J_x = (1 - \alpha)J$ and $J_y = (1 - \beta)J$. Then, from 6.1 :

$$E_{xx}^2 = E_-^2 = 16\langle Sz\rangle^2[J^2 - (1-\alpha)(1-\beta)J^2 - J^2((1-\beta)-(1-\alpha))\gamma_q + J^2(1-\alpha)(1-\beta)(1-\gamma_q^2)] \tag{12}$$

$$E_{xx}^2 = 16\langle Sz\rangle^2 J^2[\alpha(-\gamma_q + \gamma_q^2) + \beta(\gamma_q + \gamma_q^2) - \alpha\beta(1+\gamma_q^2) + 1 - \gamma_q^2] \tag{13}$$

For $Q = (100)$ and $Q = (010)$, we have $\gamma_q = -1.$, With $S_z = \frac{1}{2}$ and neglecting the second order term (factor of $\alpha\beta$), we obtain the following:

$$E_{xx} = 2J\sqrt{(2\alpha)} \tag{14}$$

Similarly, we calculated E_{yy} :

$$E_{yy} = 2J\sqrt{(2\beta)} \tag{15}$$

From the fits, we can then get the anisotropy parameters α and β for CFTD, where $J = J_0 \cdot Z_c = 6.18 \cdot 1.18 = 7.3$:

$$\alpha = \frac{E_{xx}^2}{8J^2} = 0.000184$$

$$\beta = \frac{E_{yy}^2}{8J^2} = 0.000633$$

Using the anisotropic exchange interaction coefficients J, one can obtain the spin wave dispersion of CFTD.

We did not manage however to match each peak intensity with the expected values from RPA calculations, where $I_{xx} \propto \sqrt{(\frac{J_z+J_y}{J_z-J_x})}$ and $I_{yy} \propto \sqrt{(\frac{J_z+J_x}{J_z-J_y})}$.

The ratio of the two peaks intensity should be, with the fitted coefficients α and β :

$$\frac{I_{xx}}{I_{yy}} = 1.85$$

What we find from the experiment peak intensity is

$$\frac{I_{xx}}{I_{yy}} = 0.6371$$

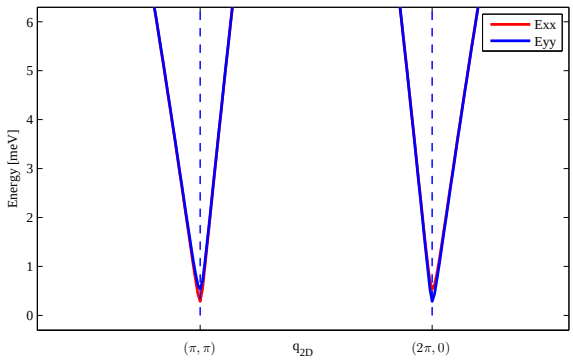

Figure 26: CFTD Dispersion - RPA calculations with fitted α and β

However, this ratio analysis is possible only if the proportionality coefficient for I_{xx} and I_{yy} are considered to be the same , which is questionable in the experiment, as the resolution function could have a different behaviour at the two excitation energies.

In order to reduce the intensity dependency on the resolution function, one can compute the Q-integrated S(E) by integrating over an interval in Q=(H,K,L). For the (010) case, integration is over the interval $H = [0.94, 1.06]$ and for the (100) case, the integration is done over the interval $K = [0.94, 1.06]$

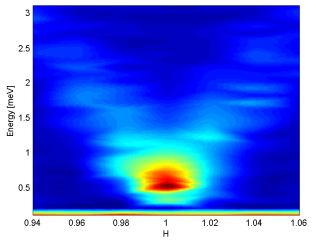

Figure 27: 2D map of the intensity in CFTD as a function of energy and of H in the Q=(H00) case

The figure 27 shows the detected intensity as a function of the energy and the value of H in $Q = (H00)$ for the range of Q over which we will integrate the intensity.

Figure 28 shows the result of the integration of the intensity over the chosen interval for both momentum transfer Q=(100) and Q=(010).

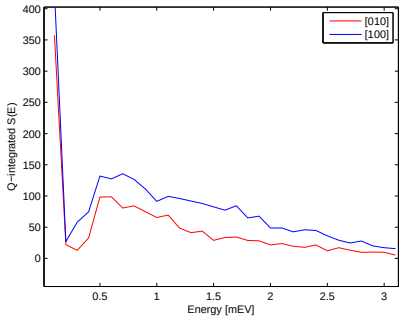

Figure 28: Q-integrated intensity as a function of energy for Q=(100) (blue curve) and Q=(010) (red curve)

The position of the c* polarisation energy gap has not shifted upon integration, and the b* energy gap is still visible. However the intensity differences between the two modes is still not what we would expect form the RPA calculations.

Another approach that could be taken to further model the obtained data could be to include the Dzyaloshinsky-Moriya (DM) mechanism, expressed as [21]: $\mathbf{D}\cdot(\mathbf{S}_1\times\mathbf{S}_2)$ This interaction would probably affect some parameters, such as the intensity, while keeping the same energy difference between the two modes.

6.4 Temperature Dependance

In addition, one can extract from the measured data the temperature dependence of the gap as well as the dynamical susceptibility of the c* polarisation as the temperature increases.

From figure 29, one can see the closing of the c* polarised spin gap (corresponding to the excitation visible in both $Q = (100)$ and $Q = (010)$) as a function of temperature. As expected, the gap goes to zero when the anisotropy is removed by the increase in temperature. From this figure also one can confirm that the strongest peak seen in the Q=(100) case corresponds to the c* polarised mode of Q=(010).

Using the fluctuation-dissipation theorem (equation 9), the dynamic susceptibility χ'' can be obtained by multiplying the measured intensity by the Bose factor : $1/(1 - e^{\frac{-E}{K_b T}})$.

Figure 30 shows the maximum intensity of the magnon excitation peak as well

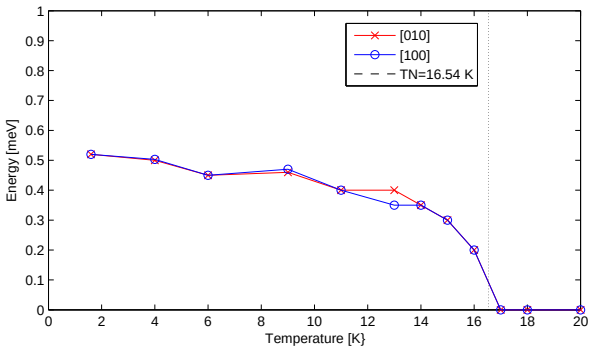

Figure 29: Magnitude of energy gap Δ of c*-polarised spin waves for momentum transfer (100) and (010)

as the calculated χ'' as a function of temperature.

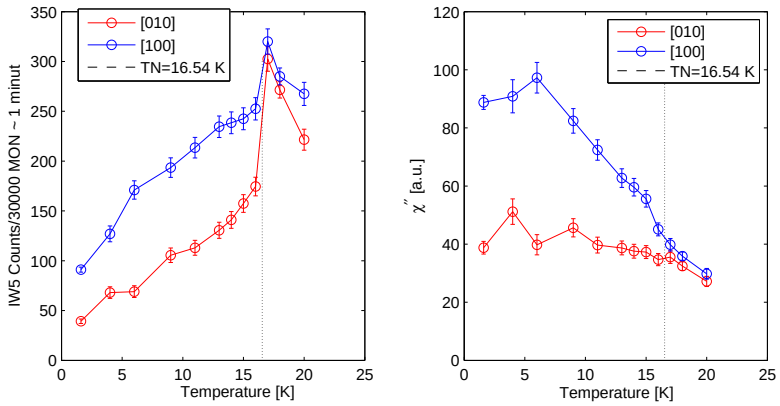

Figure 30: Intensity and χ'' of single magnon peak as a function of temperature

As expected, the dynamic susceptibility of the magnon mode decreases from base temperature to T_n and from T_n, the intensity and χ'' for both Q transfer become equal.

7 Conclusion

In summary, this work has been concerned with three different aspects of neutron scattering, the first one showing the possibilities for technical optimisation of neutron experiment via filtering while the other two are studies directly related to the magnetic studies of quantum antiferromagnetic compounds. We will briefly review all three studies in terms of results and outlook.

First, the need for optimisation of the IN1 hot neutron experiment, in order to avoid spurious signals, led us to carefully consider the absorption resonances of several neutron filters. From the time of flight measurements of the transmission of each material, statistically reliable and useful technical knowledge could be gathered about the resonances of the studied filter. Possible filter uses were discussed : thermal filter, removal of second harmonics and notch filter. From the analysis of the transmission data were extracted the parameters needed to guide a choice towards the most adapted filter in terms of material, thickness and absorption ratio with respect to the experimental range of energies. Not only does this give information about the eight materials, but the excellent agreement between our results and the averaging of the isotope data from the EDNF database also allows to rely on this database for the preliminary choice of a new filter material, using the same procedure as the analysis presented in the annex.

Second, particular choices for the La_2CuO_4 experiment have been defined, partially based on the already mentioned filter work, in order to find the best suited procedure to see the high energy excitations. Indeed, this requires both high incident energy and good resolution. Although the first part of the beamtime for this experiment was not successful in obtaining a good energy scan at $(\pi, 0)$ in the 220-360 meV energy transfer range, it nevertheless lays the ground for the continuation of the experiment, reducing the future time spent on trial and errors for the rest of the beamtime on IN1. Better known from the performed experiment are the experimental limitations of the experiment, such as the minimal 2θ angle that prevents detection of the direct beam, or the incoherent scattering detected at 340 mev energy transfer which can be removed by Erbium filtering. The knowledge number of counts that were obtained at $Q = (\pi, 0)$ around 300 meV allows estimation of the necessary time to obtain statistically significant data. The preliminary scans presented in the results show the extend of spurious signal that can be expected in the 300 meV energy transfer range. From this work, one can hope to successively set up the spectrometer to the few chosen configurations to rapidly be able to evaluate the

scans that can be obtained at the $(\pi, 0)$ point, with a La_2CuO_4 sample with a lower mosaicity than the former crystal.

Finally, the analysis of the other spin 1/2 square lattice Heisenberg antiferromagnet CFTD gave a first insight on the anisotropy of its nearest neighbour intra plane exchange constant J, using the measured energy gaps in the polarisation modes. Indeed, from the analysis of the Rita-II experimental data and the fitting of the energy gaps, the anisotropy coefficient of J_x and J_y could be evaluated to be $\alpha = 1.84 \cdot 10^{-4}$ and $\beta = 6.33 \cdot 10^{-4}$. Further studies with the inclusion of the Dzyaloshinsky-Moriya term to the Heisenberg Hamiltonian could possibly lead to a correspondence between the measured peak intensity and the intensity expected from the model. The study presented here can be used also for consistency checks of the type and strength of anisotropies in CFTD by further studies of the compound, via for example a field phase diagram or magnetization curves at low temperature. In order to get a consistent picture of the anisotropies in CFTD, the analysis of this inelastic neutron scattering data is thus a first step towards a bigger picture on the anisotropies of the system.

References

[1] F. Chen Z. J. Huang R. L. Meng Y. Y. Xue C. W. Chu, L. Gao. Superconductivity above 150 k in $hgba_2ca_2cu_3o_{8+\delta}$ at high pressures. *Nature*, 365(6444):323–325, 1993.

[2] Patrick A. Lee, Naoto Nagaosa, and Xiao G. Wen. Doping a Mott insulator: Physics of high-temperature superconductivity. *Reviews of Modern Physics*, 78(1):17–85, January 2006.

[3] Niels Bech Christensen. *Neutron scattering studies of two-dimensional antiferromagnetic spin fluctuations in insulating and superconducting S = 1/2 systems.* Riso National Laboratory, 2005.

[4] A. Mourachkine. *High-temperature superconductivity in cuprates.* Fundamental theories of physics ;. Kluwer Academic Publishers, Dordrecht, 2002.

[5] N. S. Headings, S. M. Hayden, R. Coldea, and T. G. Perring. Anomalous high-energy spin excitations in the high-T_c superconductor-parent antiferromagnet la_2cuo_4. *Phys. Rev. Lett.*, 105, 2010.

[6] R. Coldea, S. M. Hayden, G. Aeppli, T. G. Perring, C. D. Frost, T. E. Mason, S.-W. Cheong, and Z. Fisk. Spin waves and electronic interactions in la_2cuo_4. *Phys. Rev. Lett.*, 86:5377–5380, Jun 2001.

[7] M. Guarise, B. Dalla Piazza, M. Moretti Sala, G. Ghiringhelli, L. Braicovich, H. Berger, J. N. Hancock, D. van der Marel, T. Schmitt, V. N. Strocov, L. J. P. Ament, J. van den Brink, P.-H. Lin, P. Xu, H. M. Rønnow, and M. Grioni. Measurement of magnetic excitations in the two-dimensional antiferromagnetic $sr_2cuo_2cl_2$ insulator using resonant x-ray scattering: Evidence for extended interactions. *Phys. Rev. Lett.*, 105:157006, Oct 2010.

[8] N. B. Christensen, H. M. Ronnow, D. F. McMorrow, A. Harrison, T. G. Perring, M. Enderle, R. Coldea, L. P. Regnault, and G. Aeppli. Quantum dynamics and entanglement of spins on a square lattice. *Proceedings of the National Academy of Sciences*, 104:15264–15269, 2007.

[9] D. C. Mattis. *The Many-Body Problem : An Encyclopedia of exactly solved models in one dimension.* Worls scientific Publishing Co. Pte. Ltd.

[10] N. B. Christensen and H. M. Ronnow. Quantum Magnetism - a strange fish. 2007.

[11] G.C. Squires. *Thermal Neutron Scattering*. 1978.

[12] ed. A.-J. Dianoux and G. Lander. ILL neutron data booklet, 2003.

[13] Gen Shirane, Stephen M. Shapiro, and John M. Tranquada. *Neutron Scattering with a Triple-Axis Spectrometer*. Cambridge University press, 2002.

[14] B. D'Mellow, D. J. Thomas, M. J. Joyce, P. Kolkowski, Ne. J. Roberts, and S. D. Monk. The replacement of cadmium as a thermal neutron filter. *Nuclear Instruments and Methods in Physics Research Section A: Accelerators, Spectrometers, Detectors and Associated Equipment*, 577(3):690 – 695, 2007.

[15] M.B. Chadwick, M. Herman, P. Oblozinsky, et al. ENDF/B-VII.1 nuclear data for science and technology: Cross sections, covariances, fission product yields and decay data. *Nuclear Data Sheets*, 112(12):2887 – 2996, 2011. Special Issue on ENDF/B-VII.1 Library.

[16] V.F. Sears. Neutron scattering lengths and cross sections. *Neutron News 3*, 3:26–37, 1992.

[17] P. J. Brown, A. G. Fox, E. N. Maslen, M. A. O Keefe, and B. T. M. Willis. Intensity of diffracted intensities. In *International Tables for Crystallography Vol C*. John Wiley and Sons, Ltd, 2006.

[18] D. F. McMorrow D.A. Tennant. Rescal for matlab: a computational package for calculating neutron TAS resolution functions, 1995.

[19] J. Jensen A. R. Mackintosh. *Rare Earth Magnetism : Structure and Excitations*. Clarendon Press, Oxford, 1991.

[20] J. Jensen. CFTD spin waves. Unpublished, 2008.

[21] T. G. Castner and Mohindar S. Seehra. Antisymmetric exchange and exchange-narrowed electron-paramagnetic-resonance linewidths. *Phys. Rev. B*, 4:38–45, Jul 1971.

A Filter resonance curve and transmission

The data presented in 4.1 is taken form the EDNF database ([15]). The absorption cross-section is calculated as an average of each isotopes' absorption cross-section, according to their natural abundance.

The linear absorption coefficient μ is given by

$$\mu = \frac{\rho N_a}{M}\sigma_{abs}$$

with ρ the density, M the atomic molar mass, and N_a the Avogadro number. The transmission is given by:

$$T = \frac{I}{I_0} = e^{-\mu d}$$

with d the filter thickness.

A.1 Hafnium filter

A.2 Erbium filter

A.3 Indium filter

A.4 Gadolimium filter

A.5 Iridium filter

A.6 Dysprosium filter

A.7 Cadmium filter

A.8 Samarium filter

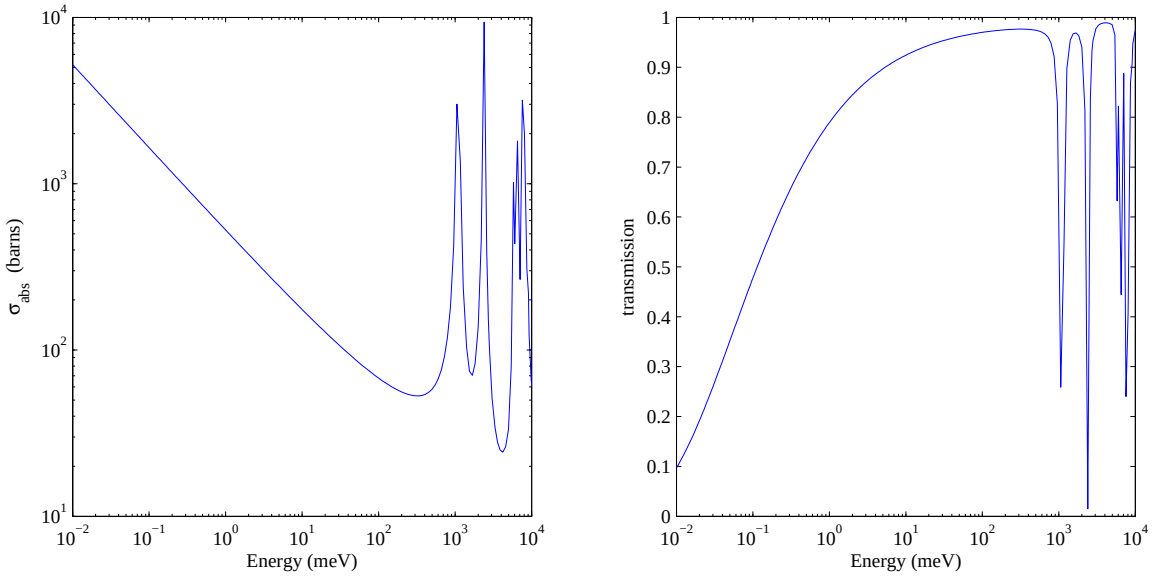

Figure 31: Hf filter absorption curve (left) and transmission curve (right), $d = 0.1$mm

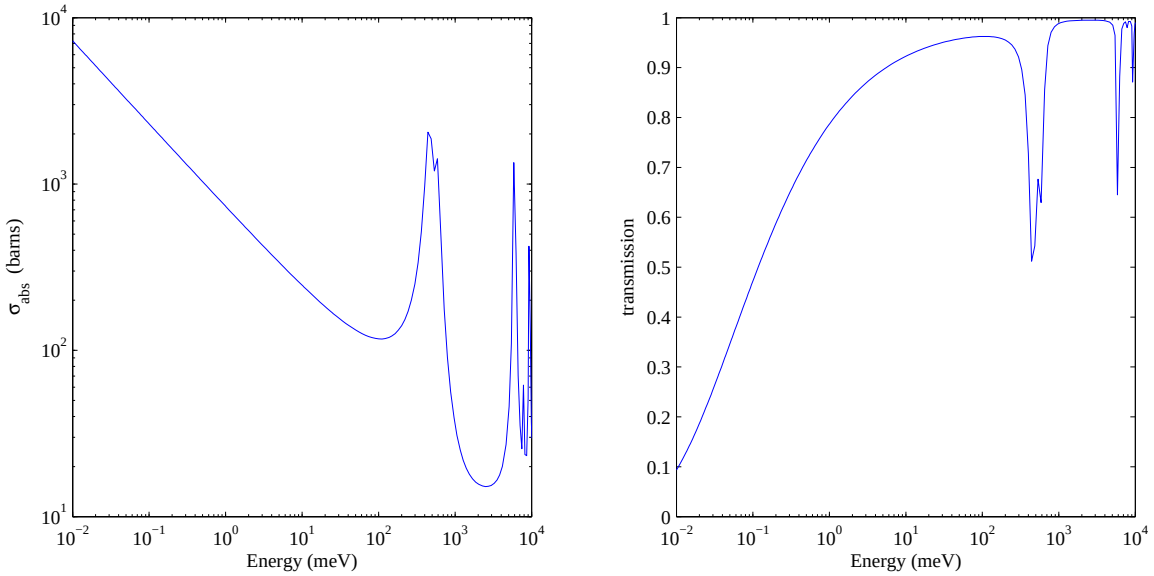

Figure 32: Er filter absorption curve (left) and transmission curve (right), $d = 0.1$mm

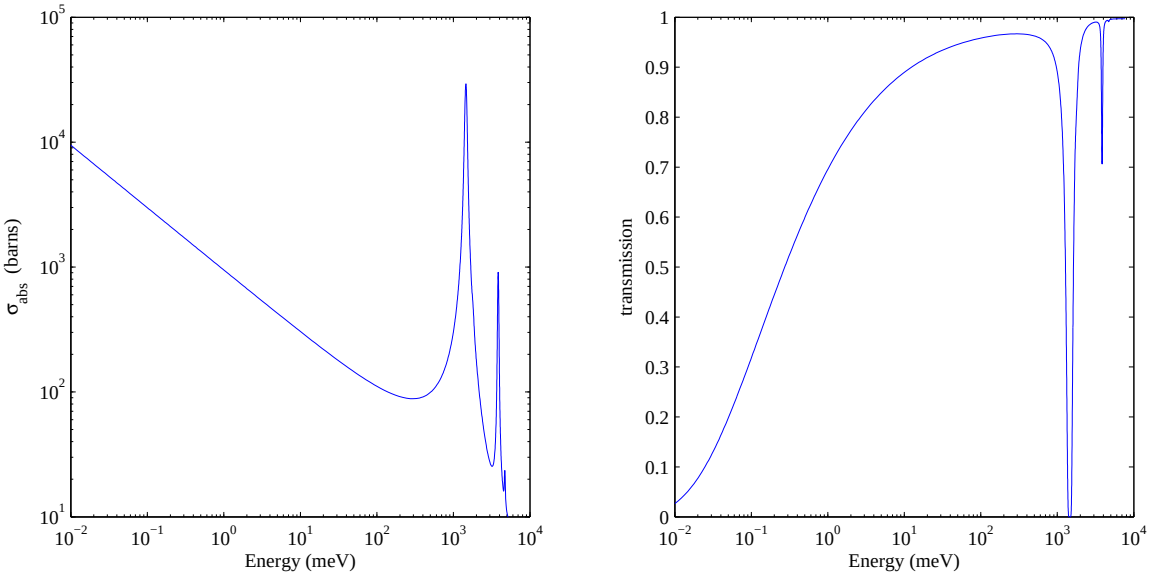

Figure 33: In filter absorption curve (left) and transmission curve (right), $d = 0.1$mm

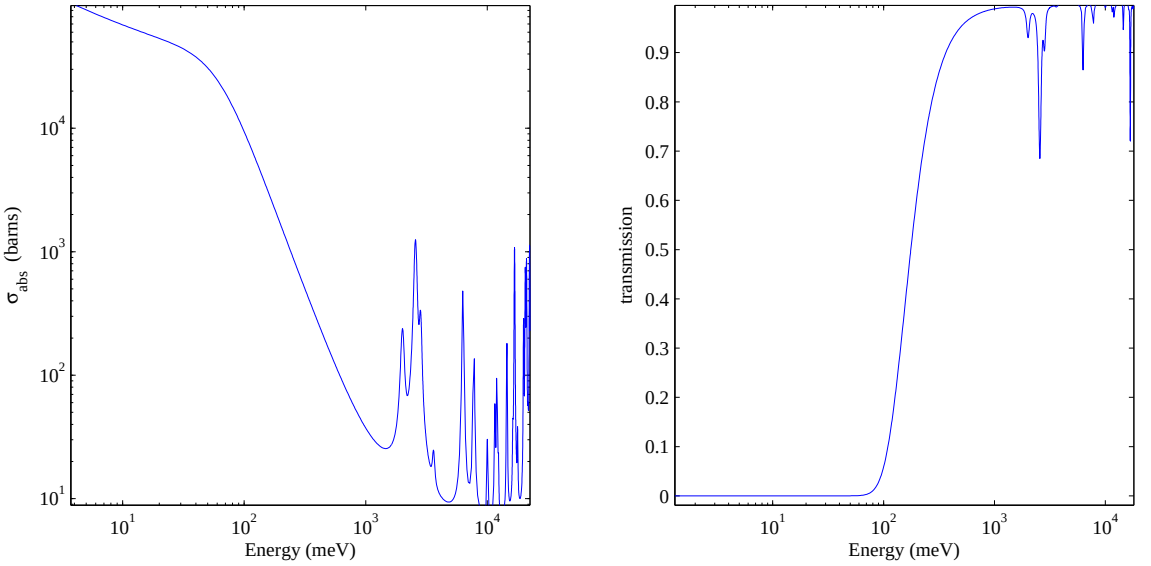

Figure 34: Gd filter absorption curve (left) and transmission curve (right), $d = 0.1$mm

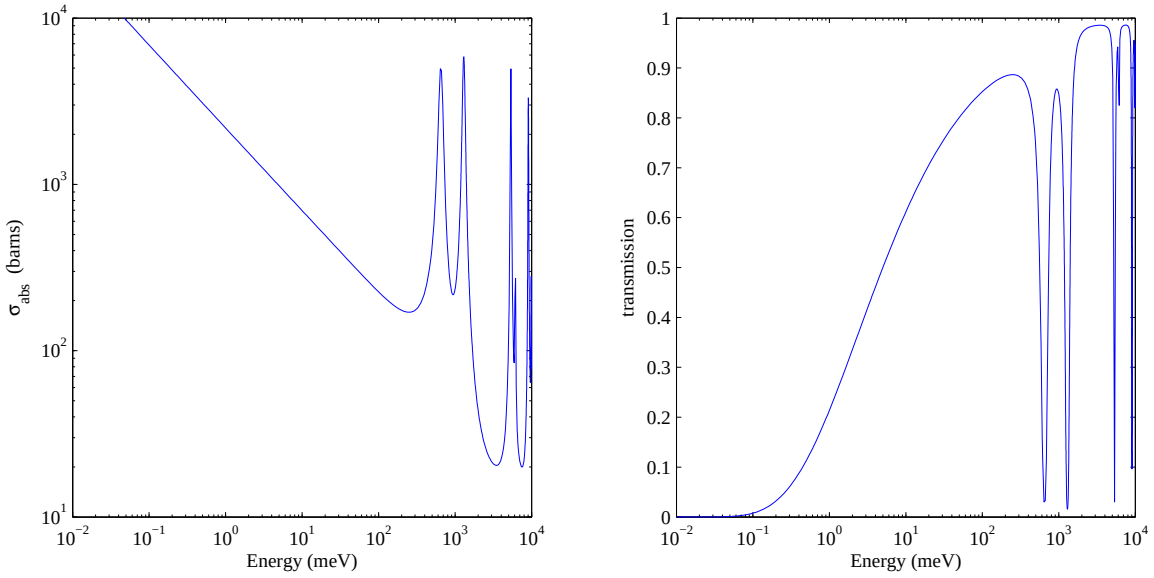

Figure 35: Ir filter absorption curve (left) and transmission curve (right), $d = 0.1$mm

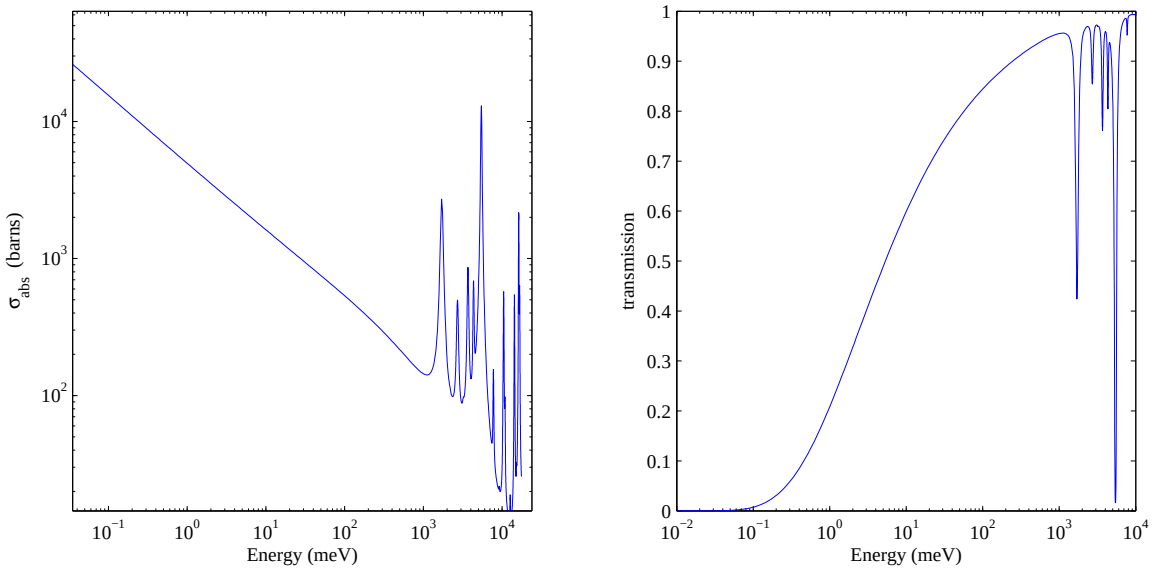

Figure 36: Dy filter absorption curve (left) and transmission curve (right), $d = 0.1$mm

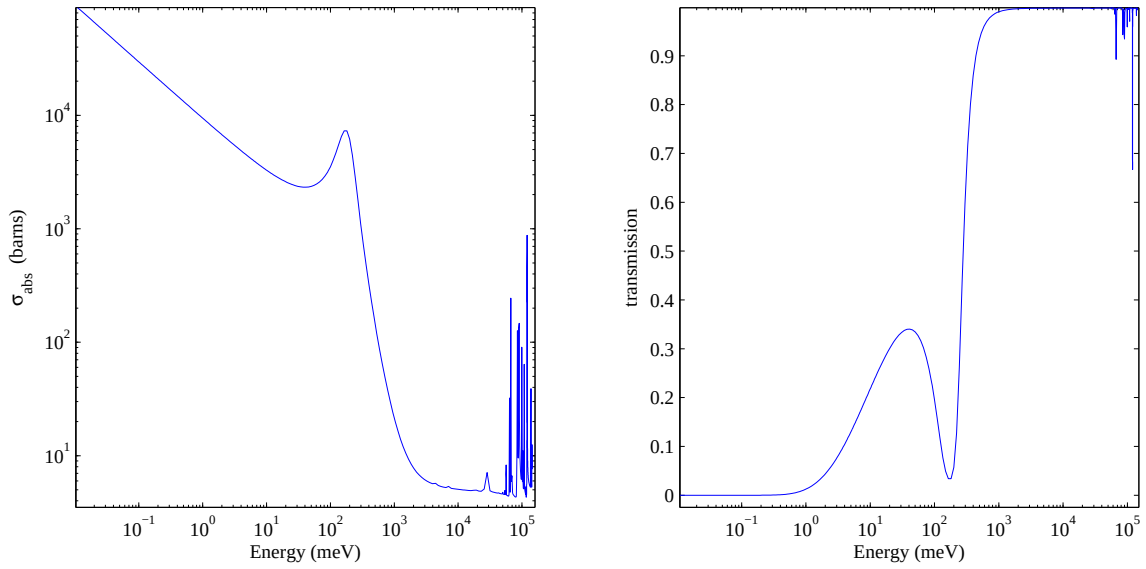

Figure 37: Cd filter absorption curve (left) and transmission curve (right), $d = 0.1$mm

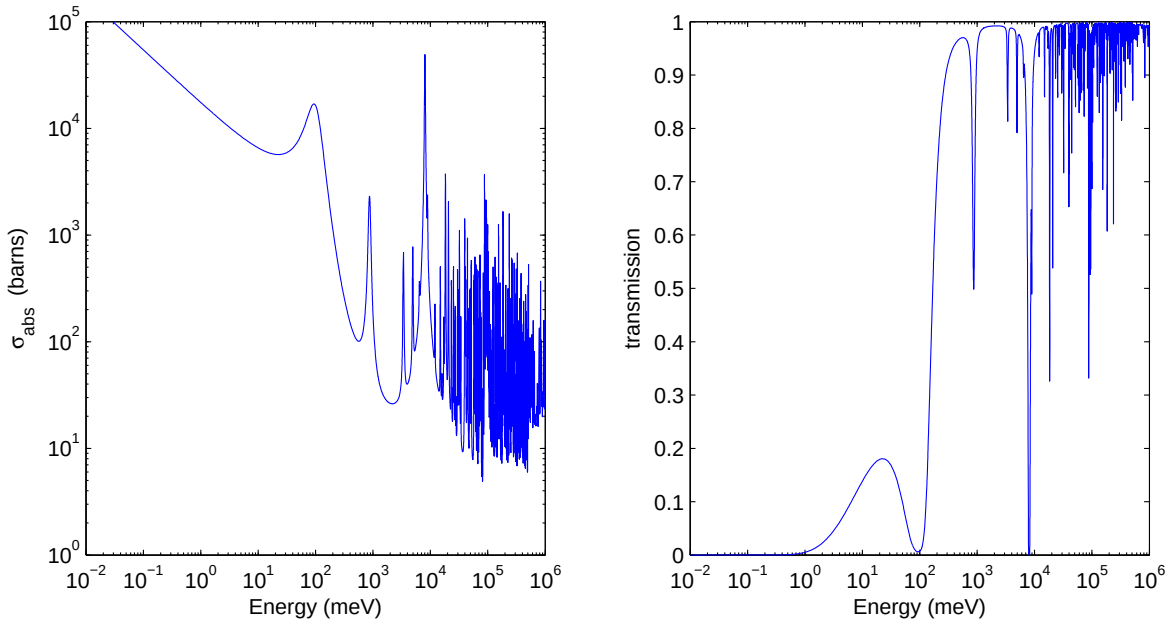

Figure 38: Sm filter absorption curve (left) and transmission curve (right), $d = 0.1$mm